

# SChanger: Change Detection From a Semantic Change and Spatial Consistency Perspective

Ziyu Zhou<sup>ID</sup>, Student Member, IEEE, Keyan Hu<sup>ID</sup>, Yutian Fang<sup>ID</sup>, and Xiaoping Rui<sup>ID</sup>

**Abstract**—Change detection is a key task in Earth observation applications. Recently, deep learning methods have demonstrated strong performance and widespread application. However, change detection faces data scarcity due to the labor-intensive process of accurately aligning remote sensing images of the same area, which limits the performance of deep learning algorithms. To address the data scarcity issue, we develop a fine-tuning strategy called the semantic change network. We initially pretrain the model on single-temporal supervised tasks to acquire prior knowledge of instance feature extraction. The model then employs a shared-weight Siamese architecture and extended temporal fusion module to preserve this prior knowledge and is fine-tuned on change detection tasks. The learned semantics for identifying all instances is changed to focus on identifying only the changes. Meanwhile, we observe that the locations of changes between the two images are spatially identical, a concept we refer to as spatial consistency. We introduce this inductive bias through an attention map that is generated by large-kernel convolutions and applied to the features from both time points. This enhances the modeling of multiscale changes and helps capture underlying relationships in change detection semantics. We develop a binary change detection model utilizing these two strategies. The model is validated against state-of-the-art methods on six datasets, surpassing all benchmark methods and achieving F1 scores of 92.87%, 86.43%, 68.95%, 97.62%, 84.58%, and 93.20% on the LEVIR-CD, LEVIR-CD+, S2Looking, CDD, SYSU-CD, and WHU-CD datasets, respectively.

**Index Terms**—Change detection (CD), deep learning, remote sensing, spatial consistency.

## I. INTRODUCTION

CHANGE detection (CD) aims to identify alterations on the Earth's surface by analyzing multitemporal remote sensing images captured at different time points over the same geographical area [1]. This technique is widely utilized in urban development monitoring [2], disaster assessment [3], and land use planning [4]. High-resolution remote sensing imagery has made remote sensing change detection (RSCD) possible, providing the clarity and detail necessary for accurate and precise analysis of changes.

Received 22 January 2025; revised 15 March 2025; accepted 23 March 2025. Date of publication 28 March 2025; date of current version 21 April 2025. This work was supported in part by the National Natural Science Foundation of China under Grant 42376180, in part by the Key Research and Development Project of Hainan Province under Grant ZDYF2023SHFZ097, and in part by the Hohai University Undergraduate Innovation and Entrepreneurship Training Program Funding under Grant 202410294199Y. (*Corresponding author: Xiaoping Rui.*)

Ziyu Zhou, Yutian Fang, and Xiaoping Rui are with the School of Earth Sciences and Engineering, Hohai University, Nanjing 211100, China (e-mail: ziyuzhou@hhu.edu.cn; yutianfang@hhu.edu.cn; ruixp@hhu.edu.cn).

Keyan Hu is with the School of Geosciences and Info-Physics, Central South University, Changsha 410100, China (e-mail: phycheor@gmail.com).

Digital Object Identifier 10.1109/JSTARS.2025.3555849

With the emergence of large-scale remote sensing datasets, deep learning technology tailored for RSCD has rapidly advanced. Fully convolutional Siamese networks [5] are widely recognized as a pioneering deep learning approach for CD, marking the beginning of extensive deep learning applications in this field. Current methods in CD encompass a variety of approaches, including convolutional neural networks (CNNs)-based techniques (e.g., Changer [6], SGSLN [7]), transformer-based approaches (e.g., ChangeFormer [8], BiT [9]), and state space model-based methods (e.g., RSM-CD [10]). However, the prerequisite for training robust and high-performing models is the availability of high-quality annotated datasets.

Acquiring and accurately aligning remote sensing images of the same region for CD tasks often requires considerable time and effort. The registration process may introduce errors due to differences in sensors or varying environmental conditions, which in turn limits the availability of usable image pairs [11], [12]. This data scarcity often results in a performance bottleneck for deep learning algorithms [13]. The size of CD datasets is much smaller than that of single-temporal datasets such as the WHU Building Dataset [14], the Inria aerial image labeling dataset [15], and general image datasets such as ImageNet (IMP) [16] and MS COCO [17]. The discrepancy in dataset sizes between single-temporal and multitemporal tasks directly affects the effectiveness of model training in CD. Pretraining on single-temporal datasets is a viable solution. However, integrating these pretrained weights into models with dual-temporal image inputs is a key challenge. During this process, it is also critical to retain as much pretrained knowledge as possible.

This study introduces SChanger, a new family of CD models designed for high-precision predictions with efficient parameters and computational complexity. To tackle data scarcity, we pretrain the SPNet on single-temporal segmentation tasks, incorporating prior knowledge of instances. For dual-temporal inputs in CD tasks, we propose a fine-tuning method called the semantic change network (SCN). It uses a shared-weight Siamese network architecture and the temporal fusion module (TFM) to retain and adapt the knowledge that was learned before. The Siamese network aligns dual-temporal features in a consistent semantic space, while the TFM resolves channel mismatches. By fine-tuning on CD tasks, the semantics of the features shift from the single-temporal segmentation domain to the dual-temporal CD domain. The spatial consistency attention module (SCAM) in the model adds an inductive bias of spatial consistency. This effectively combines dual-temporal information and focuses feature extraction on areas where building

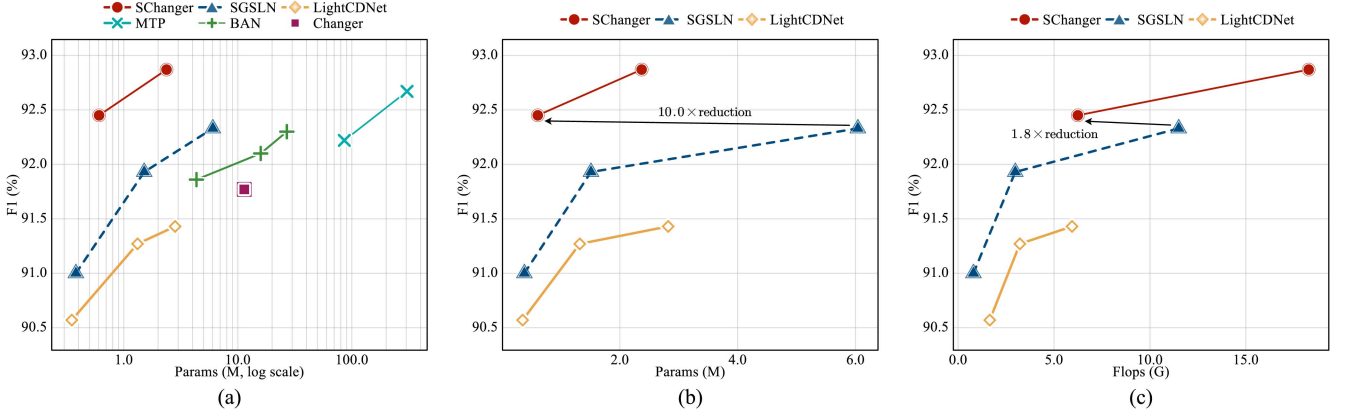


Fig. 1. Params/Flops versus performance. All performance results are obtained using a single model, with Flops calculated based on a tensor of shape  $1 \times 2 \times 256 \times 256$ . SChanger achieves significant improvements in efficiency regarding Params and Flops, while delivering comparable or superior performance on the LEVIR-CD dataset relative to previous CD models.

changes happen. The model also includes a lightweight feature enhancement module (LFEM) for feature enhancement and a multiscale fusion segmentation head (MSFSH) for multiscale information output.

We extensively evaluate SChanger on six popular CD datasets. The result for the LEVIR-CD dataset is shown in Fig. 1(a), which indicates that SChanger outperforms previous models such as BAN [32], MTP [25], Changer [6], LightCDNet [18], and SGSLN [7]. More importantly, compared to previous leading lightweight models, SChanger achieves a  $10.0\times$  reduction in parameters, as shown in Fig. 1(b), and a  $1.8\times$  reduction in floating point operations (Flops), as shown in Fig. 1(c), while maintaining similar performance. We summarize our contributions as follows.

- 1) SCN is introduced as a fine-tuning strategy for CD tasks, utilizing a shared-weight Siamese network and strategically positioned TFM modules. This design adjusts the model’s computational logic to enhance accuracy.
- 2) SCAM is designed to incorporate a shared attention map derived from large-kernel convolutions on features from both time points, introducing an inductive bias of spatial consistency. This mechanism enhances the model’s ability to capture long-range dependencies and infer relationships within change semantics.
- 3) The proposed model, SChanger, achieves notable efficiency improvements by reducing parameter count and Flops while outperforming previous state-of-the-art models in CD tasks and maintaining competitive accuracy.

## II. RELATED WORKS

### A. Pretraining and Fine-Tuning Paradigm for RSCD

In recent years, the pretraining and fine-tuning transfer learning paradigm has been widely adopted in RSCD research [6], [19]. Pretraining is the process of training the model on large-scale datasets to learn general feature representations and patterns. When task-specific datasets are limited, pretraining can significantly enhance the model’s generalization and performance. Fine-tuning builds upon the pretrained model by further

training on specific datasets, allowing the model to adapt to specific tasks or domains while reducing the high costs and risks of overfitting [20].

However, traditional pretraining datasets such as IMP lack essential domain-specific features such as buildings, roads, and vegetation, which are critical for remote sensing tasks. This limitation impedes the effective transfer of pretrained weights to these applications. Recent studies show that pretraining models from scratch on remote sensing datasets (RSP) significantly enhances performance in remote sensing tasks. For supervised pretraining, Wang et al. [21] trained architectures such as ResNet [22] and Swin Transformer [23] on the Million-AID dataset, demonstrating that RSP models outperform those using IMP. Similarly, Bastani et al. [24] showed that pretraining on the larger SATLAS dataset yielded superior results. In addition, Wang et al. [25] also achieved notable gains using multitask pretraining on the SAMRS dataset. The larger dataset size and more detailed supervision contribute to better performance. For unsupervised pretraining, Cong et al. [26] applied the masked autoencoders technique on the fMoW-Sentinel dataset, improving transfer learning performance across several downstream tasks. For single-temporal supervised learning, Zheng et al. [27] used XOR operations to generate CD image pairs from two unpaired labeled images. Simultaneously, Zheng et al. [28] introduced a resolution-scalable diffusion transformer that can generate time-series images and their corresponding semantics. We can conclude that the alignment between the visual domain of pretraining and the domain of the target task tends to positively influence the model’s performance.

While pretraining can significantly boost model performance, fine-tuning, particularly on small datasets, often causes overfitting, limiting the model’s overall effectiveness. Most transfer learning approaches assume fixed model capacity, applying fine-tuning to either the whole model or just the task-specific output layer. Recent methods have focused on expanding model capacity to better align with downstream tasks [29], [30]. Sung et al. [31] introduced the ladder side-tuning (LST) method, which enhances adaptability by freezing the base model and adding a side network for training. Li et al. [32] introduced the

BAN method, an LST extension tailored for CD tasks, optimizing dual-temporal image analysis. Although LST methods enhance a model's adaptability, they introduce too many extra parameters, leading to inefficiencies. Therefore, a key challenge is finding ways to maintain parameter efficiency while adapting to the dual-image input required for CD tasks.

Unlike data-centric approaches in single-temporal supervised learning [27], [33], where the model structure for pretraining and fine-tuning remains unchanged and only the data organization is modified, our work introduces a novel method, SCN, which adopts a model-centric perspective for transformation. By leveraging the TFM and Siamese network to expand the model's capacity for handling dual-temporal inputs and modifying the attention mechanism's computational logic during the fine-tuning phase, SCN effectively transforms single-temporal models into dual-temporal ones. This enables the utilization of pretrained weights from single-temporal data, resulting in higher performance.

### B. Deep Learning Models in RSCD

With the rapid advancements in remote sensing technologies and artificial intelligence, deep learning techniques have swiftly found broad applications in remote sensing [34], [35]. By extracting higher level feature representations of image data through multilevel processing [36], deep learning has significantly propelled the development of RSCD technology [37]. Common CD architectures include single-branch and dual-branch (Siamese) networks [38]. Single-branch networks combine two images from different times before the encoder to make processing of the inputs easier. Siamese networks, on the other hand, use a dual encoder or decoder structure with shared weights so that each image can be processed separately for better feature learning.

Typically, single-branch networks achieve image fusion by concatenating or applying absolute differencing to the input data. However, this often introduces redundancy, obscuring critical temporal variations and hindering effective extraction of meaningful change features. To address this, Papadomanolaki et al. [39] incorporated long short-term memory into CNNs. Xing et al. [18] used channel attention mechanisms. Zheng et al. [40] integrated multiscale features and multilevel semantic context. However, combining the semantic features of two images too early may not provide adequate guidance for modeling changes in features, often leading to lower accuracy. In contrast, dual-branch networks maintain separate feature extraction paths for each temporal image, providing clearer insights into changes over time. FC-Siam-conc and FC-Siam-diff networks become foundational for many subsequent CD frameworks [5]. Chen et al. [41] stated that combining dual-temporal features may introduce irrelevant background information, degrading performance. To preserve object-level differences and enhance interaction, Zhang et al. [19] combined original and differential features with channel and spatial attention mechanisms. Fang et al. [6] further improved dual-temporal interaction by exchanging feature channels between the two time points. These

methods show how important it is to improve feature interaction in Siamese networks, which do better at CD tasks than single-branch networks because they can handle inputs more independently.

Multiscale instances in remote sensing images challenge a model's ability to accurately detect and represent structures. Extending the model's receptive field is a common solution. Bandara and Patel [8] introduced the Vision Transformer (ViT) to improve long-sequence modeling. Despite ViT's strong performance in natural image tasks [23], [42], its quadratic complexity makes it expensive for high-resolution remote sensing. Furthermore, ViTs require far more training data than CNNs [43], limiting their benefits in CD tasks, especially with limited data. Depthwise convolutions to emulate ViT's ability to capture long-range dependencies, CNN models have increased convolutional kernel sizes. However, this leads to a significant rise in parameters and computational complexity. To address this, Yu [44] introduced dilated convolutions, expanding the receptive field without adding many parameters. Zhang et al. [45] further enhanced multiscale feature extraction with parallel dilated convolutions, known for their low parameter count, have also gained popularity for efficiently achieving large kernels. These methods have improved performance, as seen in models such as ConvNeXt [46] and RepLKNet [47]. CNNs remain the dominant choice for RSCD data processing, efficiently extracting feature information while maintaining parameter and computational efficiency.

Thus, this study adopts convolutional methods, with the network's overall architecture utilizing a fully Siamese network to more independently extract features from each temporal instance. The introduction of SCAM ensures effective fusion of bitemporal information. SCAM improves its accuracy in detecting changes by effectively distinguishing between altered and unaltered instances using large kernel attention [48].

## III. METHOD

In this section, we explore the modular design and overall structure of the network. First, we provide an overview of the SCAM, TFM, LFEM, and MSFSH modules, outlining their functions and contributions to the network architecture. We then explain how SPNet is built for single-temporal supervised pretraining. Next, we demonstrate how the SCN strategy enhances SPNet's ability to handle temporal changes, leading to the development of the SChanger model, an effective network for CD. Finally, we discuss the training process and key technical details of the network.

### A. Spatial Consistency Attention Module

In CD tasks, effectively capturing dual-temporal information requires incorporating inductive biases into the model. Traditional Siamese networks, which process features independently from each temporal state, fail to account for the relationships and changes between them. To address this limitation, we propose SCAM as illustrated in Fig. 2(a). SCAM improves the model's ability to detect changes by introducing an inherent inductive bias that is specific to CD. SCAM is composed of two main

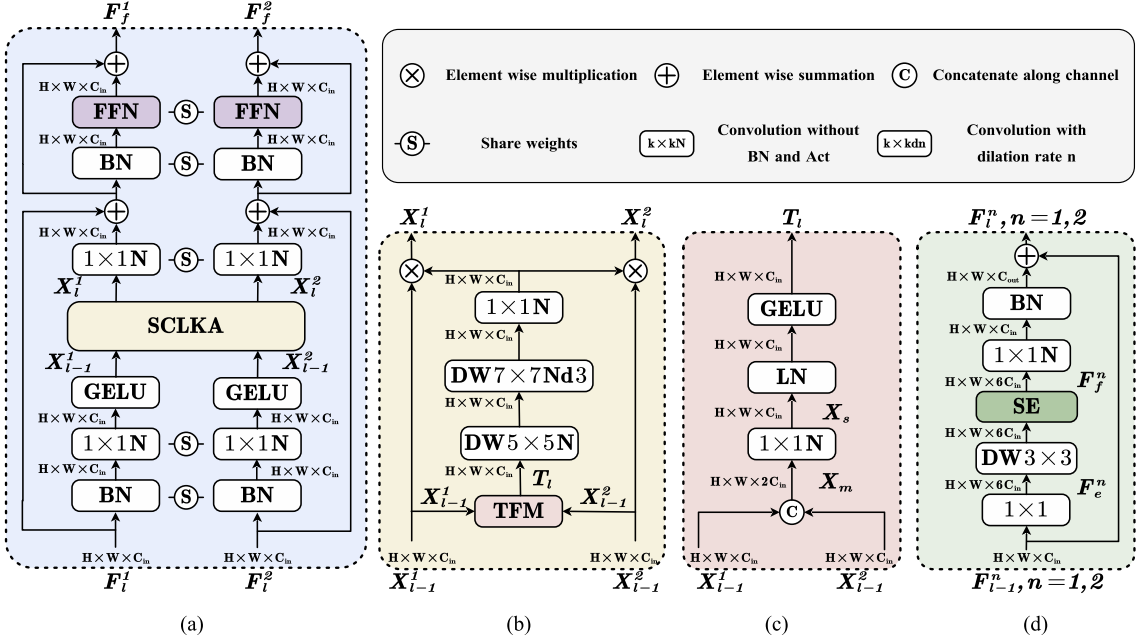


Fig. 2. Overview of the module design. (a) Illustrates each SCAM structure (see Section III-A) that facilitates dual-temporal information interaction. (b) Illustrates each SCLKA structure (see Section III-A). (c) Illustrates each TFM structure (see Section III-B), where dual-temporal features are fused. (d) Illustrates each LFEM structure (see Section III-C), where dual-temporal features are initially projected into a similar feature space.

components: spatial consistency large kernel attention (SCLKA) and the TFM. The details of SCAM and SCLKA are explained here, while TFM is covered in Section III-B.

To enhance the model's ability to capture long-range dependencies, we combine attention mechanism with large-kernel convolution. We employ a large-kernel convolution decomposition technique [48], which splits large-kernel convolutions into smaller, sequential operations. It improves the model's capacity to generate more precise attention maps, reducing the number of parameters and computational complexity. As shown in Fig. 2(b), the SCLKA module generates its output using the following steps:

$$T_l = \text{TFM}(X_{l-1}^1, X_{l-1}^2). \quad (1)$$

$$S_l = \text{DWConv}_{k_2 \times k_2, d}(\text{DWConv}_{k_1 \times k_1}(T_l)) \quad (2)$$

$$\text{Attn} = \text{Conv}_{1 \times 1}(S_l) \quad (3)$$

where  $T_l \in R^{H \times W \times C_{\text{in}}}$  represents the dual-temporal features fused by the TFM module, and  $S_l \in R^{H \times W \times C_{\text{in}}}$  denotes the spatially fused features obtained through depthwise and dilated convolutions.  $\text{Attn} \in R^{H \times W \times C_{\text{in}}}$  refers to the attention map generated through channel interaction using pointwise convolutions.  $k_1$  and  $k_2$  represent the kernel sizes of the first and second convolutions, respectively, while  $d$  denotes the dilation rate of the second convolution. For consistency and to facilitate a more meaningful comparison, the same parameter configuration as in LKA [48] is used. Specifically,  $k_1 = 5$ ,  $k_2 = 7$ , and  $d = 3$  are set to approximate a  $21 \times 21$  convolution, aiming to achieve a balance between performance and computational efficiency. In previous methods [48], attention mechanisms are applied independently to the dual-temporal images, as shown in Fig. 3(a). Due to the nature of CD tasks, the segmented

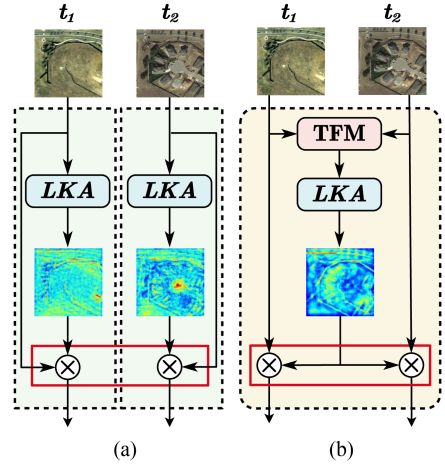


Fig. 3. Illustration of shared attention mechanism for dual-temporal images in CD. (a) Unshared attention. (b) Shared attention.

instances exist only in a single image, which leads to wasted computations for the changing instances in the other image. This also makes it more prone to introducing noise. To address this issue, an inductive bias, referred to as spatial consistency, is introduced into the model to capture changes between dual-temporal images. This bias assumes that regions experiencing changes (such as transitions from bare land to buildings) will retain their semantic identity over time. Essentially, if a region is identified as changing at one time point, it should still be recognized as a “changing” region at another time point, even though the land cover types may differ. As a result, the same “changing” attention map can be applied to both feature sets. As shown in Fig. 3(b), a shared attention map is used to influence

both time-point images. Mathematically, this is expressed as follows:

$$X_l^1 = \text{Attn} \otimes X_{l-1}^1 \quad (4)$$

$$X_l^2 = \text{Attn} \otimes X_{l-1}^2 \quad (5)$$

where  $X_{l-1}^1, X_{l-1}^2 \in R^{H \times W \times C_{\text{in}}}$  denote the input feature maps for the two temporal images, with  $\otimes$  representing elementwise multiplication. This approach enables the model to capture broader contextual information, effectively integrating CD signals while maintaining the fidelity of dual-temporal feature representations.

Finally, within the SCAM structure, the features  $F_l^1$  and  $F_l^2$  of the  $l$ th layer are successively passed through batch normalization (BN), a  $1 \times 1$  convolution, the GELU activation function, the SCLKA module, and a feed forward network to extract feature representations. In addition, we adopt a weight-sharing Siamese network structure to ensure consistent feature extraction across both temporal inputs.

### B. Temporal Fusion Module

Feature fusion in CD models often relies on simple or convolutional strategies. Simple methods such as addition, subtraction, and concatenation are vulnerable to noise, hindering accurate CD [5], [6]. Convolutional techniques attempt to address this by fusing dual-temporal features via channel concatenation, followed by convolution to improve fusion efficiency [7]. However, the normalization process after convolution still requires further discussion. Normalization techniques such as BN often overlook the unique temporal characteristics of dual-temporal features. Applying BN directly can cause inconsistencies between time steps, leading to training instability and fluctuations [49]. To mitigate this, layer normalization (LN) [50] is used to independently normalize each sample, better preserving temporal information. As shown in Fig. 2(c), the TFM generates its output through the following operations:

$$X_m = \text{concat}(X_{l-1}^1, X_{l-1}^2) \quad (6)$$

$$X_s = \text{Conv}_{1 \times 1}(X_m) \quad (7)$$

$$T_l = \text{GELU}(\text{LN}(X_m)) \quad (8)$$

where  $X_{l-1}^1, X_{l-1}^2 \in R^{H \times W \times C_{\text{in}}}$  represent the input features,  $X_m \in R^{H \times W \times 2C_{\text{in}}}$  denotes the features reduced through a pointwise convolution, and  $T_l \in R^{H \times W \times C_{\text{in}}}$  stands for the temporally fused dual-temporal features. This approach ensures the retention of temporal information embedded in the dual-temporal features.

### C. Lightweight Feature Enhancement Module

As model size increases, so does deployment complexity. To address this, we propose the LFEM, as shown in Fig. 2(d), which enhances feature extraction while maintaining computational and parameter efficiency. LFEM is based on the mobile inverted bottleneck convolution module [51]. It starts with a  $1 \times 1$  convolution to make the feature space bigger, and then it moves

on to a  $3 \times 3$  depthwise convolution to make spatial interaction. It includes a squeeze-and-excitation (SE) module [52] to adaptively reweight feature maps and concludes with a second  $1 \times 1$  convolution to project into the desired output channels. Mathematically, the LFEM at the  $l$ th stage is expressed as follows:

$$F_e^n = \text{Conv}_{1 \times 1}(F_{l-1}^n) \quad (9)$$

$$F_f^n = \text{SE}(\text{DWConv}_{3 \times 3}(F_{l-1}^n)) \quad (10)$$

$$F_l^n = \text{Conv}_{1 \times 1}(F_f^n) \oplus F_{l-1}^n \quad (11)$$

where  $F_{l-1}^n \in R^{H \times W \times C_{\text{in}}}$  represents the input features, and  $F_e^n \in R^{H \times W \times 6C_{\text{in}}}$  denotes the expanded features produced by the initial  $1 \times 1$  convolution. The output features are expressed as  $F_l^n \in R^{H \times W \times C_{\text{out}}}$ , where,  $n = 1, 2$  corresponds to the features from the first and second temporal states, respectively. The operator  $\oplus$  represents elementwise addition. The first two convolutional layers are followed by BN and the SiLU activation function. When  $C_{\text{in}} = C_{\text{out}}$ , residual connections are applied to shorten the gradient propagation path, and Dropout [53] is employed to stochastically skip network paths, introducing random depth to reduce complexity and prevent overfitting in the model.

### D. Multiscale Fusion Segmentation Head

To achieve multiscale predictive outputs and address the challenge of vanishing gradients in backpropagation through shallow layers, we introduce the MSFSH. Similar to U2-Net [54], a  $3 \times 3$  convolution is applied at each decoder layer to generate prediction maps at multiple scales. After generating these prediction maps, they are resized to the original image dimensions using bilinear interpolation. Finally, a  $1 \times 1$  convolution is employed to fuse the multiscale predictions, producing the final output.

### E. Semantic Prior Network

Viewing CD as a subset of the instances extraction task, its primary objective is to precisely identify and extract instances that have undergone alterations while disregarding instances that remain unchanged. To develop an effective model for this task, the network must first acquire prior knowledge in instance extraction.

To effectively utilize prior knowledge from instance extraction, we design and pretrain SPNet on a single-temporal supervised task. SPNet integrates LFEM (see Section III-C) and visual attention network module (VANM) [48], with MSFSH (see Section III-D) generating the final prediction mask. As shown in Fig. 4, SPNet follows a U-shaped structure [55], consisting of a five-stage encoder, a five-stage decoder, VANM, and MSFSH. The network is constructed as follows.

Both the encoder and decoder consist of two sequential LFEMs. The first adjusts input feature dimensionality, while the second extracts deeper, high-level features. An initial feature extraction module with  $3 \times 3$  convolution, BN, and SiLU

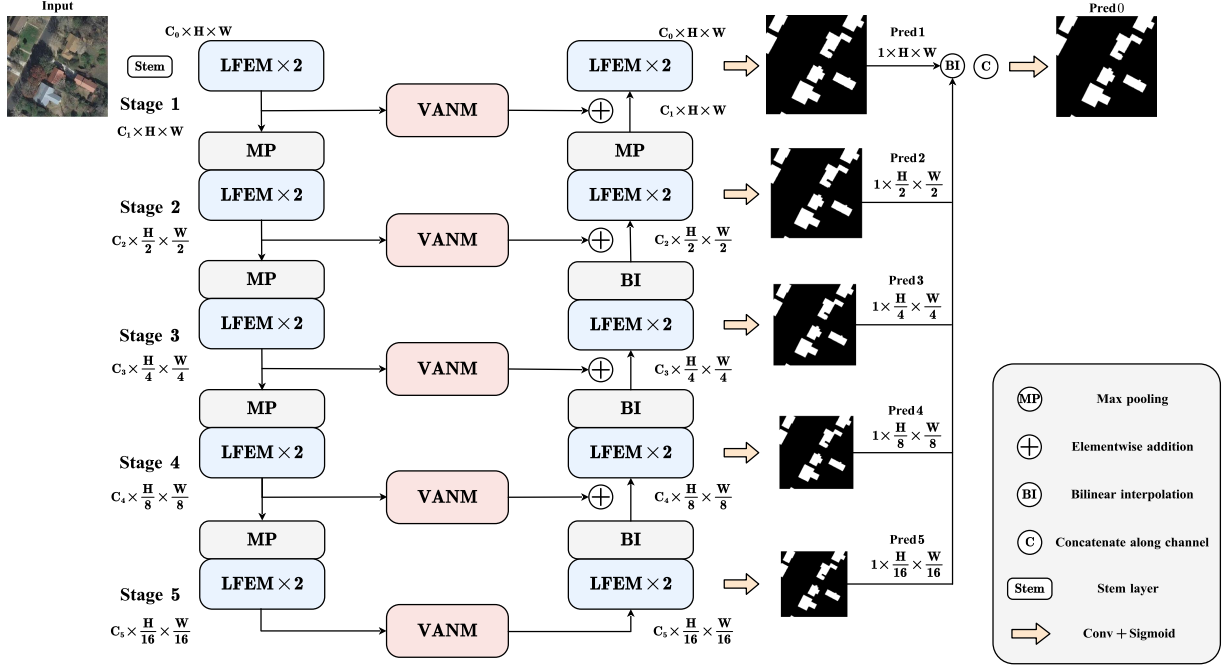


Fig. 4. Overall structure of SPNet. LFEM denotes the lightweight feature enhancement module (see Section III-C), while VANM denotes the visual attention network module [48].

activation is used before the first encoder block to expand feature dimensions. The encoder uses max pooling for downsampling, while the decoder uses bilinear interpolation for upsampling, thereby reducing both parameter count and computational complexity.

Position the VANM between the encoder and decoder to refine deeper features. For Stage 5, the decoder receives features processed by the VANM. For Stages 1 to 4, the upsampled feature map and the corresponding skip connection processed by VANM are added together to restore spatial details.

After each decoder stage, the feature maps are retained and processed through the MSFSH, with the final output generated using the sigmoid activation function.

#### F. Semantic Change Network

Semantic change refers to the process of framing the CD task as a binary instance classification problem. After acquiring prior knowledge for instance extraction, the model focuses on determining whether the detected instances have undergone change. This approach simplifies the task, making it easier for the model to learn.

To further enhance the model's ability to handle this task, we propose a fine-tuning strategy specifically designed for CD, called the SCN. Through pretraining SPNet on a single-temporal supervised task, we observe that while SPNet exhibited strong generalization capabilities, it lacks the ability to effectively capture temporal changes. To improve its performance in CD tasks, we expand the model's capacity, adapting it to better handle the intricacies of detecting changes across time.

We assume the capacity of SPNet to be fixed, consisting of  $K$  layers  $L_k$  for  $k = 1 \dots K$ . Each layer contains hidden features

$c_k \in R^{n_k}$ , where  $n_k$  represents the number of units in the  $k$ th layer. Let  $W_k$  denote the weight matrix (including bias terms) between layers  $L_k$  and  $L_{k-1}$ , such that  $c_k = f(W_k c_{k-1})$ , where  $f(\cdot)$  is a nonlinear activation function, such as the SiLU. To construct the change-augmented representation module  $F_c$ , SCN introduces a new layer,  $L_c$  (e.g., TFM), appended after the original network layers  $L_k$ , to enhance the model's capacity for CD. We consider  $L_c$  as a CD adaptation layer, enabling new combinations of existing feature transformations without significantly modifying the pretrained layers, thus adapting the model to the specific requirements of CD. The steps for SCN are as follows.

*Extending the encoder and decoder architecture:* To handle dual-temporal image inputs in CD tasks, we extend the encoder and decoder architecture using a shared-weight Siamese network. This setup allows the same encoder and decoder to process images from two different time points, ensuring both inputs utilize identical pretrained weights. The Siamese network extracts consistent feature representations from both temporal instances. Specifically, for images from  $t^1$  and  $t^2$ , the encoder and decoder generate feature representations  $c_k^1 = F_o(t^1)$  and  $c_k^2 = F_o(t^2)$ , ensuring feature consistency and enhancing performance in CD tasks.

*Dual-temporal information processing:* To effectively capture the relationships between two distinct time points in CD tasks, the shared-weight network must be capable of performing differential fusion. This is achieved through two primary mechanisms: 1) Shared attention fusion (SAF): As illustrated in Fig. 5(a), features from two separate time points,  $X_1$  and  $X_2$ , are merged using a randomly initialized TFM. The fused features are subsequently processed through pretrained SPNet layers (such as VANM), which generate an attention map. This

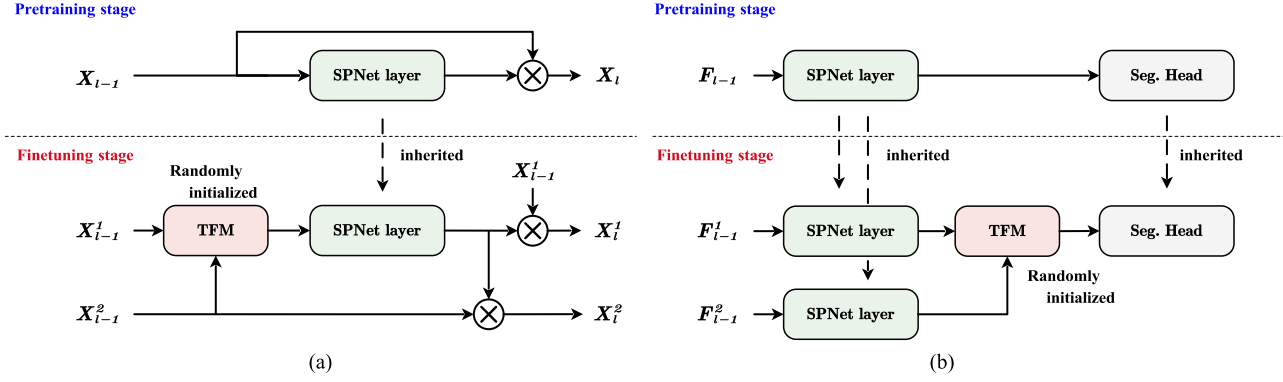


Fig. 5. Overview of SCN. (a) Represents the shared attention fusion (SAF). (b) Represents the Siamese feature adaptation (SFA). During the fine-tuning stage, the weights of the SPNet layers are inherited from the pretraining stage, and the weights of the TFM are randomly initialized.

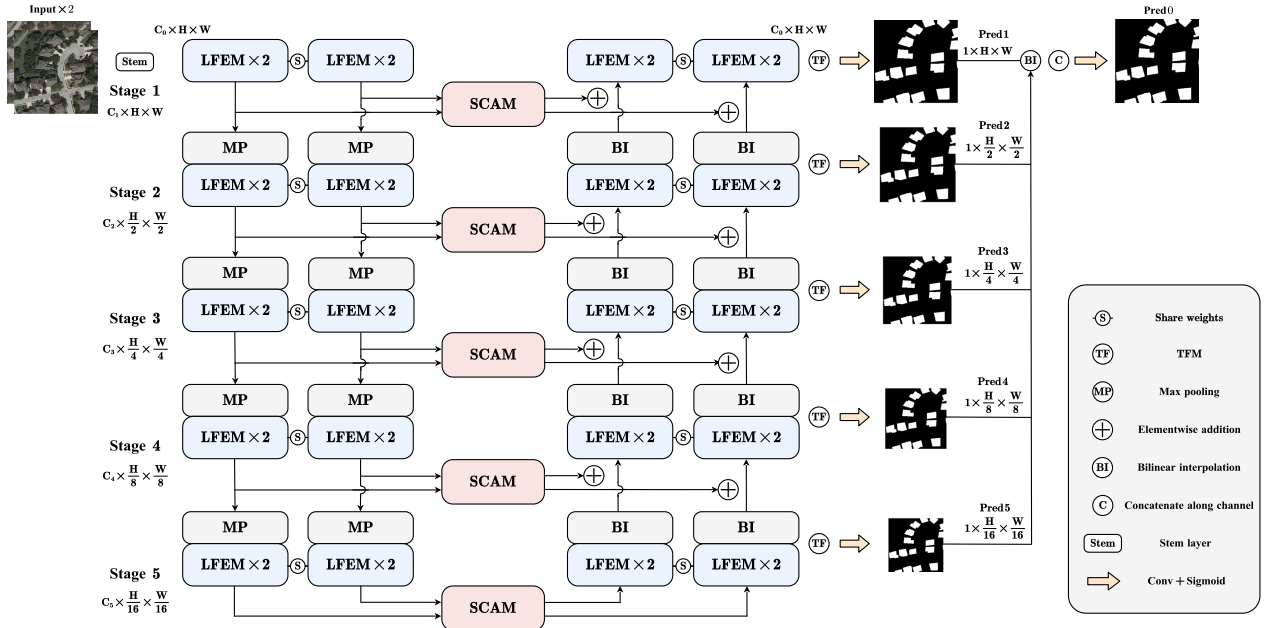


Fig. 6. Overall structure of SChanger. LFEM denotes the lightweight feature enhancement module (see Section III-C), while SCAM denotes the spatial consistency module (see Section III-A).

attention map is then applied to the feature maps from both time points, thereby enhancing its suitability for the CD task.

2) Siamese feature adaptation (SFA): As shown in Fig. 5(b), in the extended architecture leveraging the Siamese network, features  $F_1$  and  $F_2$  are processed through SPNet layers, which retain pretrained weights. A randomly initialized TFM then reduces the feature dimensions by half to match the input required for the segmentation head. Together, these mechanisms form the CD adaptation layer,  $L_c$ , enhancing the model's ability to adapt to CD tasks. This process is expressed mathematically as  $c_c = F_c(F_o(t^1), F_o(t^2))$ .

Through these refinements, the model has successfully integrated dual-temporal information processing capabilities while maintaining its structural stability. Despite the model's expansion and the introduction of new modules, the overall parameter count and computational complexity remain relatively modest, keeping the total fine-tuning cost within acceptable bounds.

The SChanger model is referred to as the SPNet augmented by SCN. As shown in Fig. 6, SChanger is designed to capture dual-temporal difference representations while minimizing computational and parameter overhead. By leveraging SCN, the pretrained weights are seamlessly incorporated into the CD architecture with only a minimal increase in parameters. This enables the network to learn more robust instance features, ultimately improving performance.

In this article, we introduce two versions of SChanger, each with different channel configurations (network width) at each stage: the standard SChanger-base and the smaller SChanger-small. Detailed configuration profiles are provided in Table I.

### G. Training Details

To enhance SChanger's capability to process multiscale information and reduce back-propagation distance, we

TABLE I  
NETWORK ARCHITECTURE FOR SCHANGER VARIANTS

Stage	downsample ratio	SChanger-small	SChanger-base
stem	1	$C_0 = 8$	$C_0 = 24$
1	1	$C_1 = 16$	$C_1 = 32$
2	2	$C_2 = 32$	$C_2 = 48$
3	4	$C_3 = 40$	$C_3 = 64$
4	8	$C_4 = 48$	$C_4 = 104$
5	16	$C_5 = 48$	$C_5 = 120$
Flops (G)		6.242	18.275
Parameters (M)		0.607	2.370
$\Delta$ Parameters (M)		0.026 (4.2%)	0.105 (4.4%)

$\Delta$  Parameters indicates the increase in parameter count resulting from the application of the SCN strategy.

incorporate deep supervision [54] to improve the model’s prediction accuracy. Deep supervision calculates the loss function at each layer of the network, generating multiscale mask outputs. Since the datasets used during both pretraining and fine-tuning stages contain a single label, the same loss function is applied consistently across stages. The loss function for each layer, as well as the total loss function, is expressed as follows:

$$l_i = \text{Bce}(y, \hat{y}) + \text{Dice}(y, \hat{y}) \quad (12)$$

$$\text{Loss} = \sum_{i=0}^5 \lambda_i \times l_i \quad (13)$$

where  $\text{Bce}(\cdot)$  and  $\text{Dice}(\cdot)$  represent binary cross-entropy and Dice loss, respectively. The term  $\lambda_i$  denotes the loss function coefficients for different layers, which we set to 1 in this study. In addition, to improve model stability, we adopt the exponential moving average [56] model with synchronized updates across layers. Formally, let the parameters of the model be denoted as  $\theta_q$ , and the updated parameters stored separately as  $\theta_k$ . The update rule for  $\theta_k$  is given as follows:

$$\theta_k \leftarrow m\theta_k + (1 - m)\theta_q. \quad (14)$$

Here,  $m \in [0, 1]$  is the momentum coefficient, set to a commonly used value (e.g.,  $m = 0.9998$ ).

For models with fewer parameters, fully fine-tuning all parameters has been demonstrated to yield better results [29]. Building on this, during the CD phase, we fully update the pretrained weights to maximize model’s effectiveness and further enhance its performance on the new task.

#### IV. EXPERIMENTS

##### A. Datasets

The basic information of the seven datasets used in the experiments is summarized in Table II. The following provides the details of each dataset:

The LEVIR-CD dataset [11], widely used for CD, contains 637 pairs of very high-resolution image patches (0.5 m per pixel) from Google Earth, each measuring  $1024 \times 1024$  pixels. It features 31 333 annotated instances of building changes, with imagery captured between 2002 and 2018. The dataset primarily focuses on transitions from grassland, soil, or construction sites

to developed buildings. For evaluation, the test set images are cropped to  $256 \times 256$  pixels.

LEVIR-CD+ dataset includes 985 pairs of images collected between 2002 and 2020, encompassing approximately 80 000 building instances. For consistency, we apply the same cropping methodology as in LEVIR-CD in our experiments.

The S2Looking dataset [57] includes 5000 image pairs, each with dimensions of  $1024 \times 1024$  pixels, and is divided into training, validation, and test sets with a 7:1:2 ratio. It features more than 65 920 annotated change instances, derived from side-looking satellite images of rural areas globally, with spatial resolutions between 0.5 and 0.8 m per pixel. The dataset presents challenges such as large viewing angles, significant illumination variations, and the complexity of rural imagery. Like the LEVIR-CD dataset, the test images are cropped to  $256 \times 256$  pixels for evaluation.

The CDD dataset [12] includes 11 pairs of Google Earth images, where seasonal variations impact mutable objects such as buildings, roads, and vehicles. This dataset poses additional challenges due to seasonal and lighting differences. The dataset is split into patches of  $256 \times 256$  pixels, with 10 000 patches for training, 3000 for validation, and 3000 for testing.

The WHU-CD dataset [14] is a large-scale resource specifically created for building CD. It consists of high-resolution image pairs, each measuring  $32207 \times 15354$  pixels, taken in Christchurch, New Zealand, beginning in 2011. With a spatial resolution of 0.2 m per pixel, the dataset captures significant postearthquake changes, particularly related to building reconstruction. To enable fair comparisons with other algorithms, the images were cropped into nonoverlapping blocks of  $256 \times 256$  pixels.

The SYSU-CD dataset [58], based in Hong Kong, contains 20000 images with a resolution of  $256 \times 256$  pixels and a spatial resolution of 0.5 m per pixel. The dataset captures a diverse array of complex change scenarios, including road expansions, the development of new urban buildings, vegetation changes, suburban growth, and groundwork before construction.

The Inria Aerial Image Labeling Dataset (IAILD) [15] comprises 360 images, each with a resolution of  $5000 \times 5000$  pixels, collected from five cities: Austin, Chicago, Kitsap, Tyrol, and Vienna. In this study, we utilize the entire training set for pretraining SPNet on the building extraction task, as the test set lacks labeled data.

##### B. Implementation Detail

To assess the performance of the proposed model, all experiments are conducted in a PyTorch 2.6 [59] environment (CUDA 11.1), utilizing a NVIDIA GeForce RTX 4090 GPU with 24 GB of memory. TorchInductor [60] is employed as the deep learning compiler to generate optimized code, accelerating both training and inference speeds. We employ the AdamW optimizer [61] with an initial learning rate of 0.0005, a cosine decay schedule, and a weight decay of 0.0002 to prevent overfitting. Data augmentation techniques include random cropping to  $256 \times 256$  pixels, horizontal/vertical flips (50% probability), random rotations, translations, and scaling (30% probability).

TABLE II  
INFORMATION OF THE SEVEN BENCHMARK DATASETS USED FOR EXPERIMENTS

Dataset	Study Site	Number of Samples	Size	Resolution	Evaluation Task
LEVIR-CD [11]	Texas	637	1024 × 1024	0.5m	object change detection
LEVIR-CD+ [11]	Texas	985	1,024 × 1,024	0.5m	object change detection
S2looking [57]	Rural regions worldwide	5,000	1,024 × 1,024	0.5-0.8m	object change detection
CDD [12]	-	16000	256 × 256	0.03-1m	binary change detection
WHU-CD [14]	Christchurch, New Zealand	1	32207 × 15354	0.3m	object change detection
SYSU-CD [58]	Hong Kong	20000	256 × 256	0.5m	binary change detection
IAILD	Austin, Chicago, Kitsap, Tyrol, Vienna	360	5000 × 5000	0.3m	building extraction

Additional augmentations such as contrast, gamma corrections, emboss effects, Gaussian noise, adjustments to hue, saturation, brightness, and motion blur are applied with a 50% probability. For CD datasets, dual-temporal images are randomly swapped with a 50% probability. The model is trained across multiple datasets for rigorous evaluation performance.

For IAILD, we start with 400 warmup epochs and a batch size of 16, followed by 4000 training epochs. For LEVIR-CD, the configuration includes 600 warmup epochs and a total of 12 000 epochs. LEVIR-CD+ requires 450 warmup epochs and 9000 total epochs. S2Looking involves 150 warmup epochs and 3000 total epochs. CDD uses 50 warmup epochs and 500 total epochs. SYSU-CD utilizes 10 warmup epochs and 450 total epochs. WHU-CD consists of 20 warmup epochs and 1000 total epochs. For all CD tasks, the models are initialized with pre-trained weights from IAILD, and a batch size of 8 is employed.

### C. Evaluation Metrics

For the CD task, we take the F1 score of the change class as the primary evaluation metric. The F1 score, along with precision and recall, are calculated as follows to evaluate the model's performance:

$$F1 = \frac{2 \times \text{Precision} \times \text{Recall}}{\text{Precision} + \text{Recall}} \quad (15)$$

$$\text{Precision} = \frac{\text{TP}}{\text{TP} + \text{FP}} \quad (16)$$

$$\text{Recall} = \frac{\text{TP}}{\text{TP} + \text{FN}} \quad (17)$$

where TP denotes true positives, TN refers to true negatives, FP indicates false positives, and FN represents false negatives.

### D. Compared Methods

To evaluate the performance of the proposed SChanger model, we compare it against several leading CD methods. Current CD methods in deep learning fall into three major categories: models based on CNNs, models based on convolutional attention mechanisms, and models based on transformer architectures. For the CNN-based methods, we select several classic and SOTA algorithms for comparison, including FC-EF [5], FC-Siam-Conc [5], FC-Siam-Diff [5], UNet++MSOF [37], ChangeStar2 (R-50) [33], and ChangerEx [6]. These methods rely on CNNs to extract spatial features for accurate CD. For the attention-based convolutional methods, we include models such as DTCDSNC [62], IFN [19], SGSLN/512 [7], HANet [63],

TABLE III  
COMPARISON OF THE RESULTS WITH OTHER SOTA METHODS ON LEVIR-CD

Methods	Year	P. (%)	R. (%)	F1 (%)
FC-EF [5]	2018	86.91	80.17	83.40
FC-Siam-Conc [5]	2018	91.99	76.77	83.69
FC-Siam-Diff [5]	2018	89.53	83.31	86.31
DTCDSNC [62]	2020	88.53	86.83	87.67
ChangeFormer [8]	2020	92.59	89.68	91.11
IFN [19]	2020	<b>94.02</b>	82.93	88.13
BiT-18 [9]	2021	89.24	89.37	89.31
HANet [63]	2023	91.21	89.36	90.28
ChangerEx [6]	2023	92.97	90.61	91.77
SGSLN/512 [7]	2023	93.07	91.61	92.33
LightCDNet [18]	2023	92.43	90.45	91.43
CGNet [64]	2023	93.15	90.90	92.01
C2FNet [65]	2024	<b>93.69</b>	90.04	91.83
SRCNet [66]	2024	92.63	<b>91.72</b>	92.24
CACG-Net [67]	2024	92.16	92.41	92.29
MutSimNet [69]	2024	90.46	93.59	92.00
MTP [25]	2024	-	-	<b>92.67</b>
SChanger-small	-	92.93	<b>91.96</b>	<b>92.45</b>
SChanger-base	-	<b>93.18</b>	<b>92.61</b>	<b>92.87</b>

Color convention: First (red), Second (blue) and Third (bold).

CGNet [64], C2FNet [65], SRCNet [66], STANet [11], CACG-Net [67], and intelligent-BCD [68]. These models integrate attention mechanisms to enhance accuracy and robustness by focusing on the most relevant features. Among transformer-based approaches, we select ChangeFormer [8], BiT [9], MutSimNet [69], and TransUNetCD [70]. These methods leverage the self-attention mechanism of transformers to capture long-range dependencies in images, which significantly enhances their performance in CD tasks.

### E. Main Results

The experimental results on the LEVIR-CD dataset, as shown in Table III, highlight the superior performance of the proposed SChanger model. SChanger-small achieves an F1 score of 92.45%, and SChanger-base reaches 92.87%. These results represent the SOTA performance on this dataset. Compared to the previous best-performing model, MTP, SChanger improves the F1 score by 0.20%. In addition, it outperforms the previous best lightweight model, SGSLN/512, improving precision, recall, and F1 score by 0.11%, 1.00%, and 0.54%, respectively. Fig. 7 presents the detection results for some examples from the LEVIR-CD dataset. It is evident that the outcomes produced by our proposed model align more closely with the corresponding ground truth compared to the results from other models.

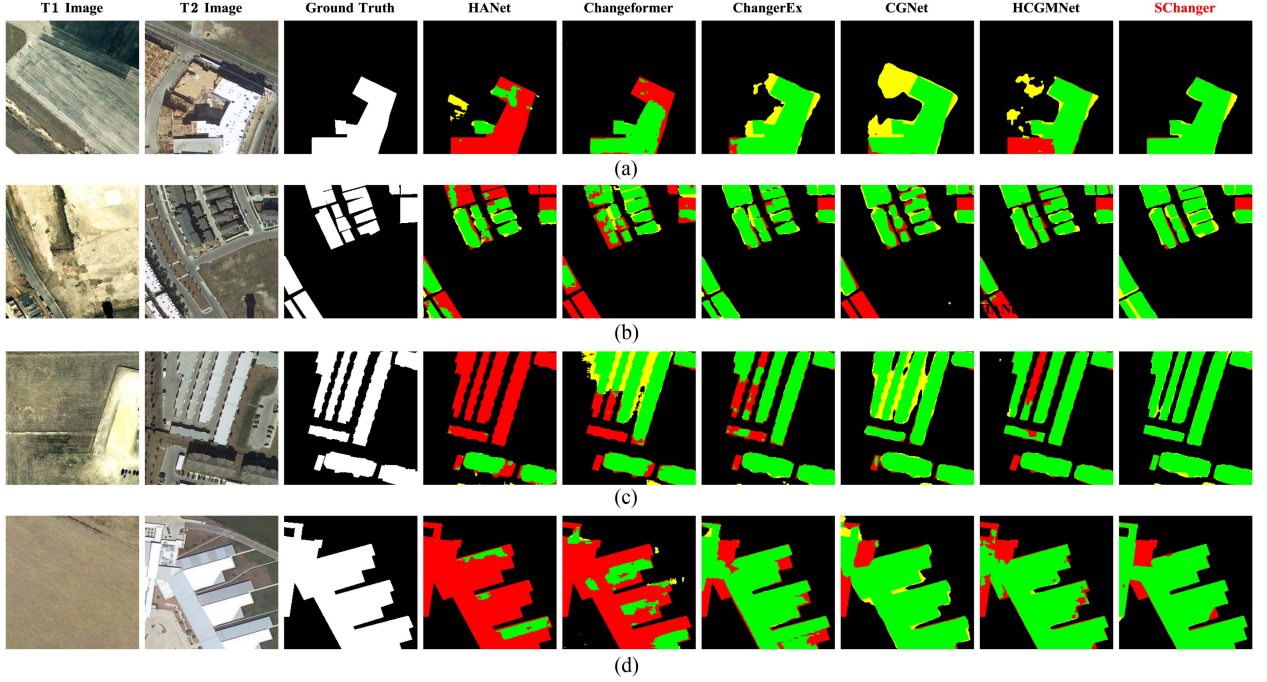


Fig. 7. Qualitative evaluation results of SOTA comparison methods on the LEVIR-CD dataset. TP (green), TN (black), FP (yellow), and FN (red).

TABLE IV  
COMPARISON OF THE RESULTS WITH OTHER SOTA METHODS ON LEVIR-CD+

Methods	Year	P. (%)	R. (%)	F1 (%)
FC-EF [5]	2018	61.30	72.61	66.48
FC-Siam-Conc [5]	2018	66.24	81.22	72.97
FC-Siam-Diff [5]	2018	74.97	72.04	73.48
UNet++MSOF [37]	2019	<b>85.90</b>	67.10	75.34
DTCDSN [62]	2020	80.36	75.03	77.60
STANet [11]	2020	74.62	84.54	79.27
BiT-18 [9]	2021	82.74	82.85	82.79
Intelligent-BCD [68]	2022	<b>93.80</b>	79.90	<b>86.29</b>
CGNet [64]	2023	81.46	<b>86.02</b>	83.68
SChanger-small	-	84.53	<b>87.93</b>	<b>86.20</b>
SChanger-base	-	<b>85.28</b>	<b>87.61</b>	<b>86.43</b>

Color convention: First (red), Second (blue) and Third (bold).

TABLE V  
COMPARISON OF THE RESULTS WITH OTHER SOTA METHODS ON S2LOOKING

Method	Year	P. (%)	R. (%)	F1 (%)
FC-EF [5]	2018	<b>81.36</b>	8.95	7.65
FC-Siam-Conc [5]	2018	68.27	18.52	13.54
FC-Siam-Diff [5]	2018	<b>83.29</b>	15.76	13.19
ChangeFormer [8]	2020	72.82	56.13	63.39
DTCDSN [62]	2020	68.58	49.16	57.27
BiT-18 [9]	2021	72.64	53.85	61.85
HANet [63]	2023	61.38	55.94	58.54
ChangerEx [6]	2023	73.59	60.15	66.20
CGNet [64]	2023	70.18	59.38	64.33
C2FNet [65]	2024	<b>74.84</b>	54.14	62.83
ChangeStar2 [33]	2024	69.20	<b>66.50</b>	<b>67.80</b>
SChanger-small	-	70.63	<b>65.93</b>	<b>68.20</b>
SChanger-base	-	70.94	<b>67.09</b>	<b>68.95</b>

Color convention: First (red), Second (blue) and Third (bold).

Table IV shows the comparison of accuracy results on the LEVIR-CD+ dataset. SChanger-small records an F1 score of 86.20%, with SChanger-base raising it to 86.43%. These results outperform the CNN-based Intelligent-BCD by 0.14% and the Transformer-based BiT by 3.64%. Despite LEVIR-CD+ being more challenging than LEVIR-CD, SChanger-base's performance only drops by 6.44% and SChanger-small's by 6.25%, outperforming models such as CGNet (8.33%), BiT (7.47%), and DTCDSN (10.07%). This highlights SChanger's robustness and adaptability in handling complex changes.

As shown in Table V, our method performs strongly on the S2Looking dataset. SChanger-base achieves an F1 score of 68.95% and SChanger-small scores 68.20%, surpassing the previous SOTA method, ChangeStar2, by 1.15% and 0.40%, respectively. Due to significant visual differences in rural bitemporal images, the S2Looking dataset presents challenges. SChanger's prior knowledge of building extraction from IAILD and spatial

consistency inductive bias enables more accurate, efficient detection change, resulting in improved performance on these complex scenes. Fig. 8 shows detection results from the S2looking dataset, where our model's outcomes align more closely with the ground truth than those of other models.

Table VI highlights the performance of our method on the CDD dataset. SChanger-small achieves an F1 score of 95.75%, while SChanger-base reaches 97.62%, reflecting a 0.12% improvement over the second-best method, ChangeStar2. These results demonstrate the model's robustness in handling scenarios involving seasonal changes.

Table VII shows the results on the SYSU dataset, which includes multiple categories. The comparison reveals that SChanger-small achieves the highest F1 score of 84.58%, while SChanger-base follows with a score of 84.17%, surpassing the previous best method, CACG-Net, by 1.23%. It is noteworthy

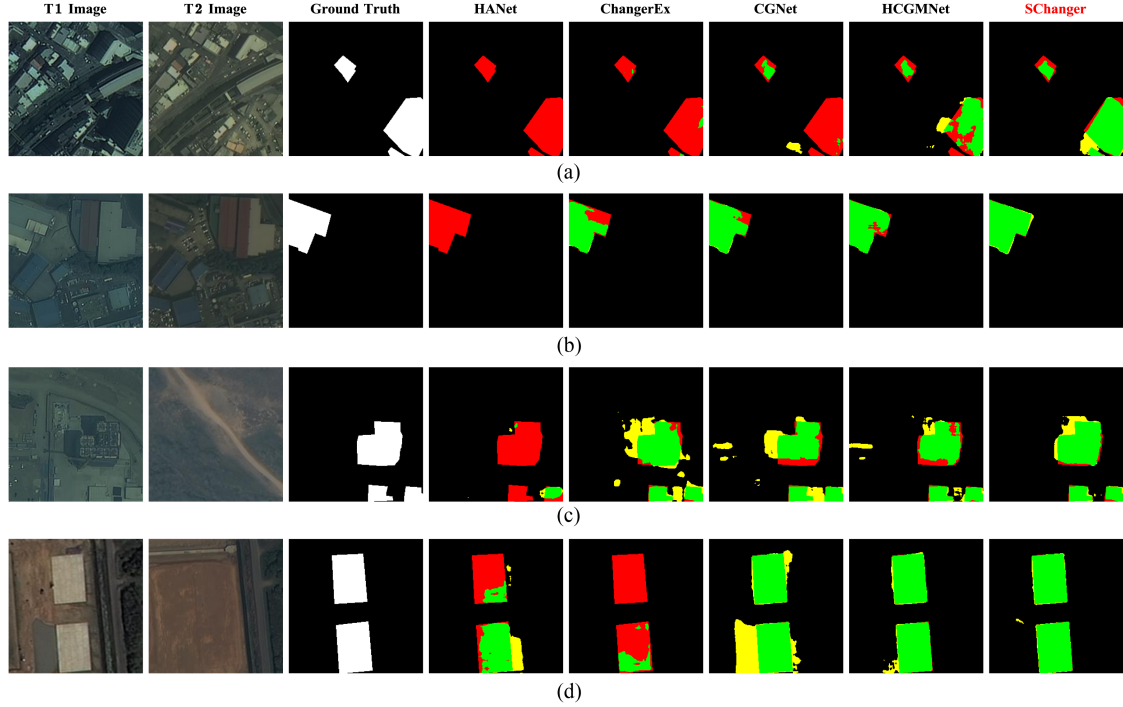


Fig. 8. Qualitative evaluation results of SOTA comparison methods on the S2looking dataset. TP (green), TN (black), FP (yellow), and FN (red).

TABLE VI  
COMPARISON OF THE RESULTS WITH OTHER SOTA METHODS ON CDD

Methods	Year	P. (%)	R. (%)	F1 (%)
FC-EF [5]	2018	60.90	58.30	59.57
FC-Siam-Conc [5]	2018	70.90	60.30	65.17
FC-Siam-Diff [5]	2018	76.20	57.30	65.41
UNet++MSOF [37]	2019	86.68	76.53	81.29
IFN [19]	2020	90.56	70.18	79.08
HANet [63]	2023	92.89	85.87	89.23
CGNet [64]	2023	93.67	95.82	94.73
C2FNet [65]	2024	95.46	<b>96.41</b>	<b>95.93</b>
ChangeStar2 [33]	2024	<b>98.00</b>	<b>97.00</b>	<b>97.50</b>
SChanger-small	-	<b>95.48</b>	96.02	95.75
SChanger-base	-	<b>97.95</b>	<b>97.28</b>	<b>97.62</b>

Color convention: First (red), Second (blue) and Third (bold).

TABLE VIII  
COMPARISON OF THE RESULTS WITH OTHER SOTA METHODS ON WHU-CD

Methods	Year	P. (%)	R. (%)	F1 (%)
FC-EF [5]	2018	83.50	86.33	84.89
FC-Siam-Conc [5]	2018	84.02	87.72	85.83
FC-Siam-Diff [5]	2018	90.86	84.69	87.67
DTCDSN [62]	2020	63.92	82.30	71.95
IFN [19]	2020	91.44	89.75	90.59
BIT-18 [9]	2021	90.30	90.36	90.33
HANet [63]	2023	88.30	88.01	88.16
CGNet [64]	2023	<b>94.47</b>	<b>90.79</b>	<b>92.59</b>
SChanger-small	-	<b>95.36</b>	<b>91.04</b>	<b>93.15</b>
SChanger-base	-	<b>94.62</b>	<b>91.83</b>	<b>93.20</b>

Color convention: First (red), Second (blue) and Third (bold).

TABLE VII  
COMPARISON OF THE RESULTS WITH OTHER SOTA METHODS ON SYSU-CD

Methods	Year	P. (%)	R. (%)	F1 (%)
FC-EF [5]	2018	76.47	75.17	75.81
FC-Siam-Conc [5]	2018	73.67	76.75	75.21
FC-Siam-Diff [5]	2018	76.28	75.30	75.79
IFN [19]	2020	79.59	75.58	77.53
STANet [11]	2020	70.76	<b>85.33</b>	77.36
HANet [63]	2023	78.71	76.14	77.41
CGNet [64]	2023	<b>86.37</b>	74.37	79.92
SGSLN/512 [7]	2023	84.76	81.45	83.07
C2FNet [65]	2024	75.44	80.67	77.97
MutSimNet [69]	2024	82.91	81.73	82.34
CACG-Net [67]	2024	82.42	<b>84.30</b>	<b>83.35</b>
SChanger-small	-	<b>85.05</b>	<b>84.11</b>	<b>84.58</b>
SChanger-base	-	<b>86.35</b>	82.09	<b>84.17</b>

Color convention: First (red), Second (blue) and Third (bold).

that SChanger-small outperforms SChanger-base, likely due to the simpler nature of the dataset. The smaller model is less prone to overfitting, allowing it to generalize better, while the larger model, with its increased complexity, may be more susceptible to overfitting.

Table VIII highlights the performance of our method on the WHU-CD dataset, which is widely used for CD tasks. SChanger-small achieves an F1 score of 93.15%, demonstrating its effectiveness in identifying and detecting changes across different categories in the dataset. Meanwhile, SChanger-base performs slightly better, with an F1 score of 93.20%. Despite the minimal difference between the two models, the results showcase the robustness of our approach in handling complex tasks.

TABLE IX  
PERFORMANCE OF SCHANGER ON LEVIR-CD DATASET UNDER FEW-SHOT LEARNING

Sample Ratio	5%	10%	20%	30%	100%
<b>Rand. Init.</b>	86.76	89.54	90.74	91.25	92.54
<b>SCN-based</b>	91.26	91.57	92.04	92.47	92.87
<b>Improvement</b>	↑ 4.50	↑ 2.03	↑ 1.30	↑ 1.22	↑ 0.33

The F1 scores (%) are highlighted.

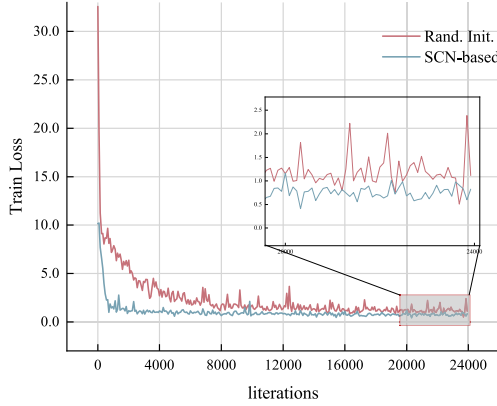


Fig. 9. Training loss curves: Random initialization versus SCN-based initialization.

#### F. Few-Shot Learning

To evaluate SCN’s impact on the generalization capability of SCHANGER, we conduct a few-shot learning experiment on the LEVIR-CD dataset, reducing the training samples from 30% to 5% and assessing the model’s performance on the test set. Leveraging SCN, SCHANGER effectively acquires prior knowledge. As presented in Table IX, with 5%, 10%, 20%, 30%, and 100% of the training samples, SCHANGER achieves F1 scores of 91.26%, 91.57%, 92.04%, 92.47%, and 92.87%, respectively. These results underscore the critical role of SCN in enhancing SCHANGER’s performance in few-shot learning, with significant F1 score improvements compared to random initialization, by 4.50%, 2.03%, 1.30%, 1.22%, and 0.33%, further validating the effectiveness and importance of SCN.

Based on the data presented in Fig. 9, the training loss curves of randomly initialized and SCN-based weights under the 5% label condition were compared, with the descent rate of the loss value serving as an approximate measure of the convergence rate. It is evident that SCN outperforms random initialization in terms of convergence, accelerating the early stages of convergence and ultimately achieving a lower final convergence loss.

#### G. Transferability Evaluation

A transferability evaluation of SCHANGER is conducted alongside various benchmark models. The models are initially trained using the LEVIR-CD dataset, and their performance is then assessed on the WHU-CD dataset. The accuracy metrics are shown in Table X.

TABLE X  
ACCURACY COMPARISON ON THE CROSS-DOMAIN CD FROM LEVIR-CD TO WHU-CD

Method	P (%)	R (%)	F1 (%)
IFN [19]	<b>78.92</b>	21.73	34.08
BiT-18 [9]	64.38	33.83	44.35
TransUNetCD [70]	72.28	38.47	50.21
FCCDN [41]	70.91	41.24	52.15
SGSLN/512 [7]	73.46	<b>42.83</b>	<b>54.11</b>
SCHANGER-small	<b>88.42</b>	<b>52.01</b>	<b>65.49</b>
SCHANGER-base	<b>87.59</b>	<b>64.87</b>	<b>74.54</b>

Models trained on the LEVIR-CD dataset experience a significant drop in performance when applied to the WHU dataset. This decline can be attributed to differences in imaging conditions and scene characteristics between the two datasets. Among all the evaluated models, SCHANGER achieves the highest F1 score on the WHU dataset, demonstrating its superior transferability. Notably, SCHANGER-base shows a 20.43% improvement over SGSLN/512, highlighting that SCHANGER is capable of extracting more generalized change features, rather than being constrained to a single scene.

#### H. Efficiency Test

The performance of the SCHANGER model is compared with other CD models, focusing on the number of parameters, computational load, throughput, and F1 score measured on the LEVIR-CD dataset. Throughput is assessed by recording the start and end times using CUDA’s event function to ensure precise timing. To improve accuracy, the experiment is conducted three times, with each iteration processing 1000 samples. The first 10 samples from each run are discarded to eliminate the impact of warmup time. Table XI illustrates that SCHANGER-small, with just 0.607 M parameters and 6.242 G Flops, attains an F1 score of 92.45%, highlighting its efficient design. On the other hand, SCHANGER-base, which has 2.370 M parameters and 18.275 G Flops, achieves a higher F1 score of 92.87%. Remarkably, SCHANGER-small delivers a similar F1 score to SGSLN/512 while reducing the parameter count by nearly 90% and Flops by 50%, alongside comparable throughput, demonstrating its computational efficiency.

### V. ABLATION STUDY

#### A. Efficacy of MSFSH

In the SCHANGER model, the MSFSH is crucial for detecting subtle changes by capturing multiscale information and shortening the gradient backpropagation path. As shown in Table XII (Experiment ID 1 and 2), the SCHANGER model with MSFSH outperforms the baseline, achieving a 0.38% F1 score improvement, demonstrating the importance of MSFSH.

#### B. Efficacy of SCAM

In the SCHANGER model, SCAM enhances the receptive field and improves the interaction between bitemporal information streams. From a quantitative perspective, as shown in Table XII,

TABLE XI

EFFICIENCY COMPARISON OF DIFFERENT METHODS: NUMBER OF FLOPS AND THROUGHPUT COMPUTED USING A TENSOR OF SHAPE  $2 \times 3 \times 256 \times 256$ 

Method	Year	Params. (M)	Flops (G)	Throughput (Sample/s)	LEVIR-CD F1 (%)
FC-EF [5]	2018	1.350	3.121	416.55	83.40
FC-Siam-Diff [5]	2018	1.350	4.275	294.52	86.31
FC-Siam-Conc [5]	2018	1.546	4.879	288.19	83.69
IFN [19]	2020	35.995	79.036	131.09	88.13
ChangeFormer [8]	2020	41.015	138.639	43.78	91.11
CGNet [64]	2023	38.989	87.683	189.07	92.01
SGSLN/512 [7]	2023	6.036	11.524	96.23	92.33
C2FNNet [65]	2024	16.257	62.130	77.69	91.83
SRCNet [66]	2024	5.195	8.373	86.57	92.24
SChanger-small (ours)	-	0.607	6.242	85.91	92.45
SChanger-base (ours)	-	2.370	18.275	73.93	92.87

TABLE XII

ABLATION STUDY OF DIFFERENT MODULES ON THE LEVIR-CD DATASET

ID	MSFSH	VANM	SCAM	SCN	Params. (M)	Flops (G)	P (%)	R (%)	F1 (%)	$\Delta$ F1 gains (%)
1	-	-	-	-	1.857	14.505	92.87	91.09	91.97	-
2	✓	-	-	-	1.897	14.593	93.14	91.56	92.35	↑ 0.38
3	✓	✓	-	-	2.304	18.381	91.77	92.97	92.37	↑ 0.40
4	✓	-	✓	-	2.370	18.275	93.05	92.03	92.54	↑ 0.57
5	✓	-	✓	✓	2.370	18.275	93.06	92.67	92.87	↑ 0.90

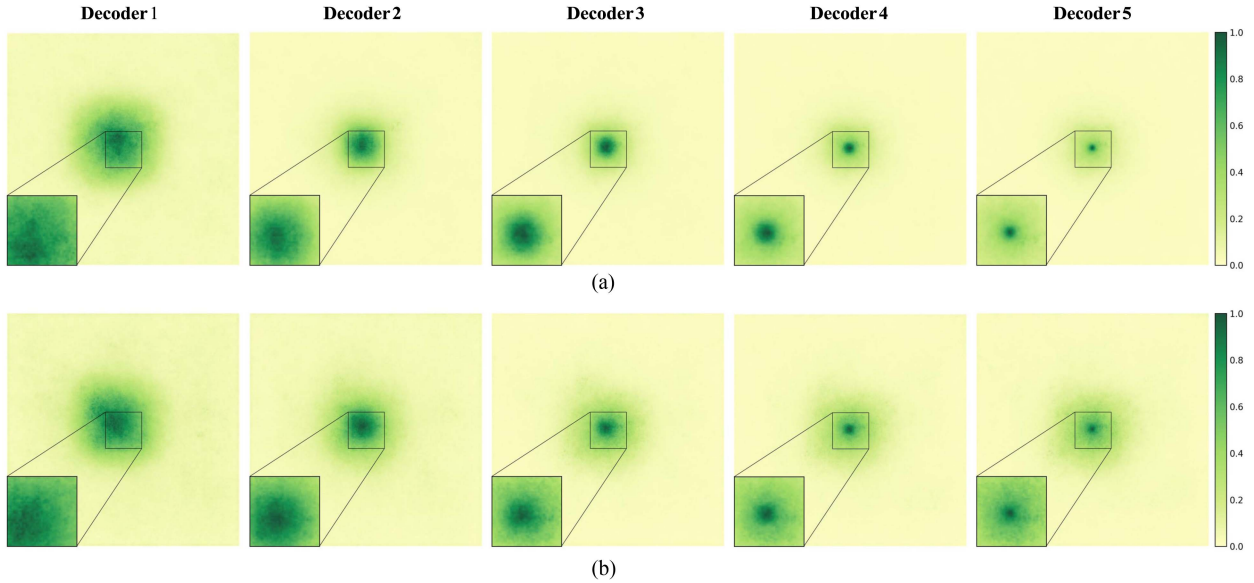


Fig. 10. Effective receptive field of (a) w/o SCAM model (Experiment ID 2), (b) w/ SCAM model (Experiment ID 4).

VANM increases recall by 1.41%, but reduces precision by 1.37% (Experiment ID 2 and 3), likely due to its sensitivity to irrelevant features. However, incorporating a spatial consistency inductive bias (Experiment ID 3 and 4) improves both recall and precision while maintaining similar parameters and Flops. This results in a 0.57% increase in the F1 score, underscoring the importance of feature interaction.

From a qualitative perspective, the use of large-kernel convolutions leads to larger effective receptive fields (ERFs) [71]. We analyze Experiment ID 2 and 4, and Fig. 10 visually demonstrates how the ERFs evolve across different decoder stages in both the baseline model and the baseline with

SCAM. Our observations are as follows: 1) As the decoder layers become deeper, the network focuses more on localized features, and the receptive field becomes more constrained. 2) SCAM significantly expands the ERF in the deeper decoder stages, which is crucial for dense prediction tasks in CD. These insights suggest that SCAM's use of large-kernel convolutions enhances the model's ability to capture long-range dependencies, leading to improved accuracy and feature representation.

Furthermore, to better understand SCAM's effectiveness and superior performance, we use Grad-CAM [72] to analyze and compare Experiment ID 3 and 4. As illustrated in Fig. 11, the heatmap analysis of the two decoder layers in the SChanger

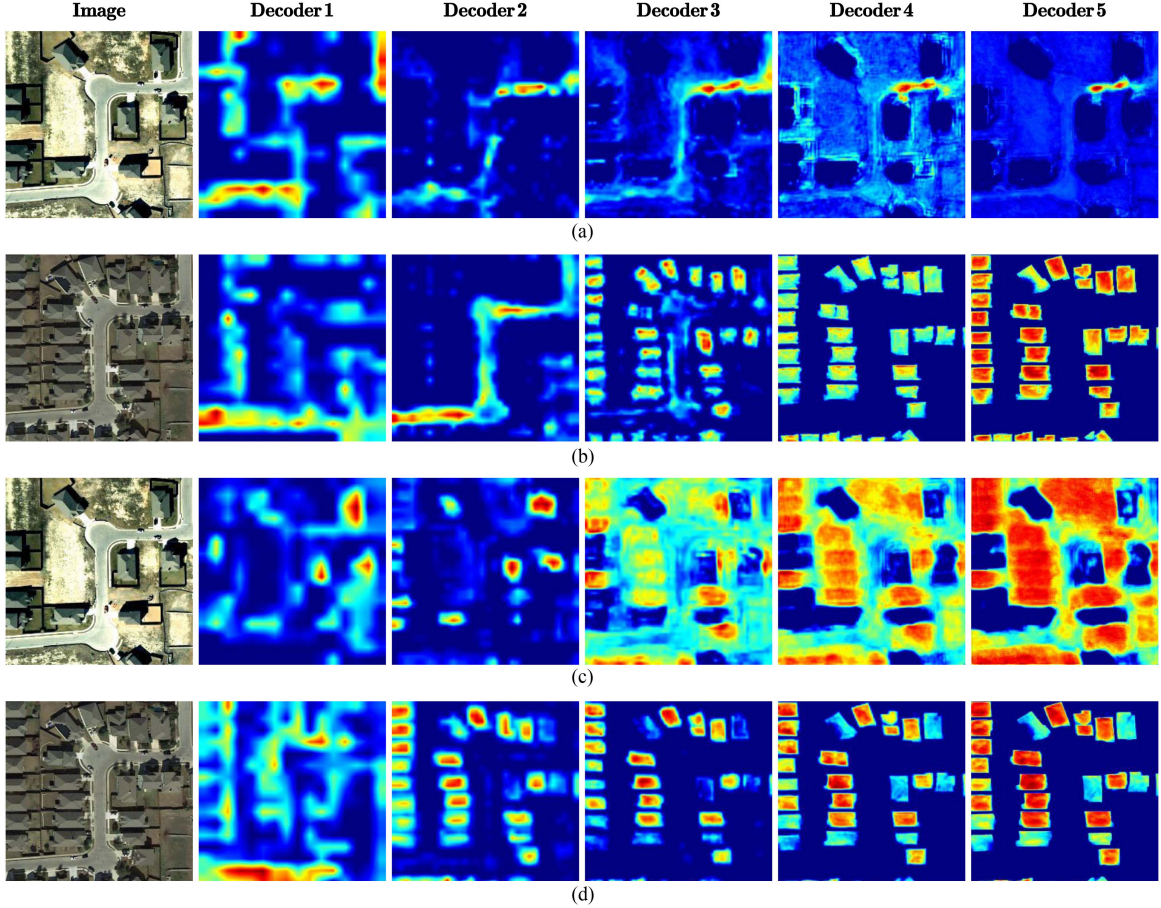


Fig. 11. Grad-CAM visualization results (focusing on all pixels in the change category). The visualization comparison is made between the VANM (Experiment ID 3) and SCAM (Experiment ID 4). The panels show: (a) VANM for t1, (b) VANM for t2, (c) SCAM for t1, and (d) SCAM for t2.

model highlights key differences. 1) The VANM variant uniformly focuses on buildings and their surroundings but struggles to distinguish between changed and unchanged structures, while SCAM accurately identifies and focuses on the changed buildings. 2) VANM overly emphasizes noisy road features, whereas SCAM filters out noise and concentrates on changes related to buildings. These findings emphasize SCAM’s advantage in CD, improving overall accuracy.

Fig. 12 provides a visual comparison of SChanger variants on the LEVIR-CD dataset, showcasing their ability to detect and localize changes. For large-scale buildings, as shown in Fig. 12(a) and (b), the SCAM model excels at preserving fine details and edges, avoiding internal gaps. In cases where trees partially obstruct buildings, as in Fig. 12(c), SCAM effectively distinguishes between actual and obstructed instances, reducing false positives. In complex environments, as shown in Fig. 12(d), SCAM demonstrates superior performance in localizing changed buildings, showcasing improved precision, robustness, and localization. These results confirm SChanger’s effectiveness in accurately extracting change information.

### C. Efficacy of SCN

The primary objective of training the SChanger model using the SCN strategy is to effectively integrate prior knowledge for

instance extraction. To evaluate its impact, we load the pretrained weights and conduct an ablation study focusing on the two key components of SCN, namely, SFA and SAF. As shown in Table XIII, the results demonstrate that both the SFA and SAF modules significantly enhance the model’s performance. When combined, these modules yield a 1.11% improvement in the F1 score, underscoring their effectiveness in adapting pretrained models for the CD task. In comparison to models with random initialization, as shown in Table XII (Experiments ID 4 and 5), incorporating prior knowledge and fine-tuning results in a 0.64% increase in recall and a 0.33% improvement in the F1 score. These findings highlight the crucial role of prior knowledge in enhancing the model’s ability to handle complex changes.

### D. Evaluation of Fusion Strategies

To evaluate the TFM module, comparative experiments are conducted using different fusion strategies on the LEVIR-CD dataset. We ensure fairness by keeping the parameter counts and computational complexity similar across all strategies. We apply the SCN strategy and compare four fusion methods: direct addition, absolute subtraction, TFM-BN (using BN), and TFM-LN (using LN). As shown in Table XIV, compared to the widely-used baseline of absolute subtraction, TFM-LN improves recall by 0.69% and the F1 score by 0.14%. In addition, compared to

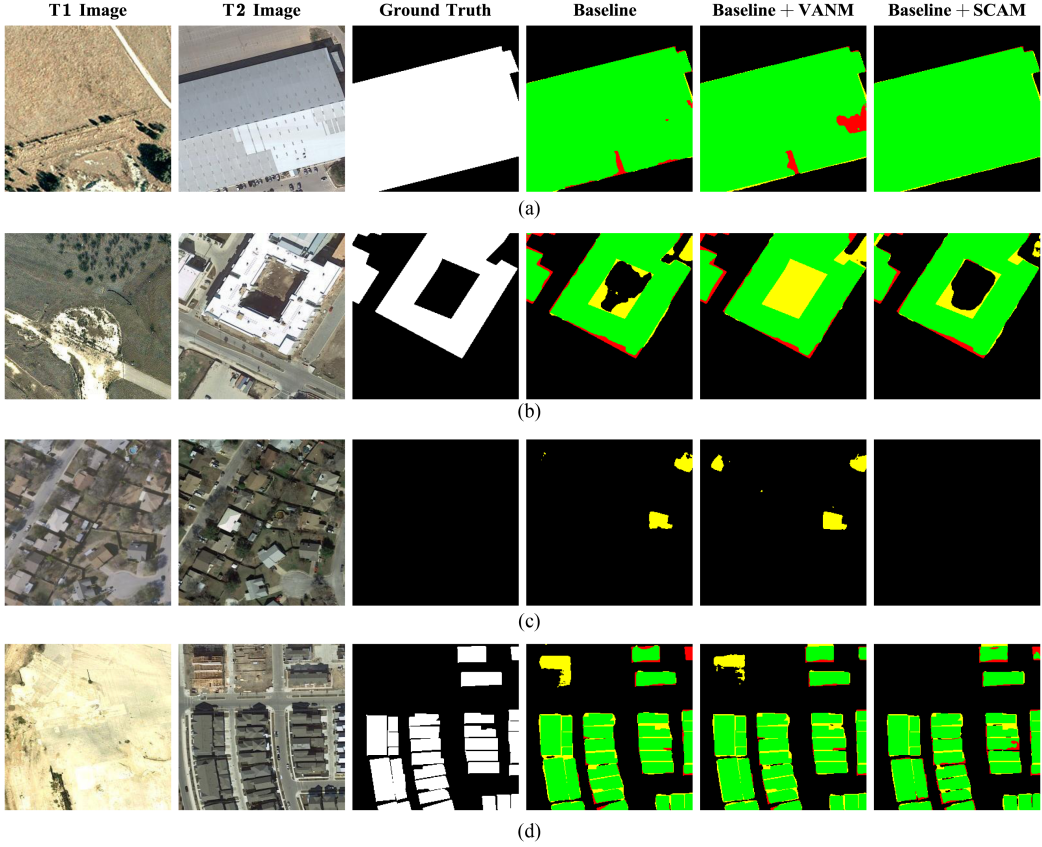


Fig. 12. Error analysis for SChanger on LEVIR-CD. The rendered colors represent TP (green), FP (yellow), and FN (red).

TABLE XIII  
ABLATION STUDY OF DIFFERENT STRATEGIES USED IN SCN ON THE LEVIR-CD DATASET

ID	SAF	SFA	Param. (M)	Flops (G)	P (%)	R (%)	F1 (%)	$\Delta$ F1 gains (%)
1	-	-	2.267	18.261	92.42	91.11	91.76	-
2	-	✓	2.304	18.381	92.55	91.74	92.15	↑ 0.39
3	✓	-	2.333	18.155	92.69	91.86	92.27	↑ 0.51
4	✓	✓	2.370	18.275	93.06	92.67	92.87	↑ 1.11

TABLE XIV  
COMPARISON OF DIFFERENT FUSION STRATEGIES ON THE LEVIR-CD DATASET

Fusion Strategy	Params. (M)	Flops (G)	P (%)	R (%)	F1 (%)
Addition	2.265	17.860	93.16	92.00	92.57
Absolute Subtraction	2.265	17.860	93.50	91.98	92.73
TFM-BN	2.370	18.303	<b>93.53</b>	91.29	92.40
TFM-LN	2.370	18.275	93.06	<b>92.67</b>	<b>92.87</b>

The best values are highlighted in bold.

TFM-BN, TFM-LN improves recall by 1.38% and the F1 score by 0.47%. These results confirm that LN preserves temporal information and enhances overall performance in CD tasks.

## VI. DISCUSSION

### A. Negative Transfer

In an effort to further enhance the generalization capability of SChanger, the SPNet model is pretrained on a larger dataset. The aim is to improve its performance across diverse tasks.

However, the results are unexpectedly contrary to expectations. The model is pretrained on the WHU-Mix dataset [73], which includes regions from the Kitsap, Tyrol, and Vienna areas of the IAILD dataset, as well as a diverse set of regions from five continents. The pretraining configuration is consistent across all experiments.

To evaluate whether the model successfully learns key building features, a cross-domain test is conducted using the Massachusetts Buildings Dataset (MA) [74]. The results show that the pretrained model has indeed acquired useful knowledge

TABLE XV  
CROSS-DOMAIN EVALUATION OF SPNET AND FINE-TUNED SCORES FOR SCN PRETRAINED MODEL ON DIFFERENT DATASETS

Init. Method	MA	LEVIR-CD	SYSU-CD	WHU-CD
Rand. Init.	-	92.54	83.95	92.90
IAILD	27.17	92.87	84.17	93.20
WHU-Mix	59.29	92.56	84.05	92.26
Change	↑ 32.13	↓ 0.31	↓ 0.12	↓ 0.94

for building extraction. As illustrated in Table XV, the model pretrained on the WHU-Mix dataset outperforms the IAILD-pretrained model by 32.13% in the cross-domain experiment on the MA dataset, highlighting the model's ability to generalize and extract key building features.

However, when fine-tuned using the SCN method on CD datasets, the performance of the WHU-Mix pretrained model is found to be inferior to that of the IAILD pretrained model across all three datasets: LEVIR-CD, SYSU-CD, and WHU-CD. Specifically, the performance decreases by 0.31%, 0.12%, and 0.94%, respectively. Furthermore, on the WHU-CD dataset, the model pretrained on WHU-Mix even performs worse than the randomly initialized model. This unexpected discrepancy in performance prompts the occurrence of negative transfer [75]. Given that the IAILD pretrained model outperforms the randomly initialized model, it is unlikely that the building extraction task itself hinders the CD task. One possible explanation is that the WHU-Mix dataset contains a significant amount of irrelevant data, which may require data cleaning or the application of data generation techniques to reduce the influence of low-quality samples and increase the number of high-quality samples.

### B. Expectations and Limitations

Bitemporal CD is a foundational task in the broader field of CD, focused on identifying and extracting areas that have undergone changes by comparing dual-temporal image data. Various methods have been proposed to address this task, with dual-branch networks emerging as a widely adopted approach. In this article, we introduce SCN, a novel method that enhances bitemporal CD performance by leveraging more data from single-temporal images. The SChanger model trained using SCN demonstrates strong performance across multiple binary CD and object CD tasks. However, with the continuous advancements in Earth observation technologies, the availability of multitemporal image data has increased significantly. As a result, processing visual data across multiple time points has become an increasingly essential challenge for more complex CD tasks.

While dual-branch networks attempt to iteratively process multitemporal images by taking two images at a time, this approach has a significant limitation. Specifically, for n images, the encoder stage feature extraction is wasted n-2 times, leading to inefficiencies in processing and underutilization of available data. In addition, binary CD methods commonly used in these networks do not provide clarity on the categories of changes,

which limits the model's ability to extract meaningful and actionable information from multitemporal datasets.

## VII. CONCLUSION

We propose the SChanger model for CD, integrating SCAM, TFM, LFEM, and MSFSH, trained with the SCN strategy. SCAM incorporates spatial consistency to enhance bitemporal fusion. TFM employs LN to stabilize training by normalizing features while preserving temporal information. The SCN strategy utilizes fully pretrained weights from single-temporal tasks, facilitating accurate change identification. These components collectively contribute to the superior performance of SChanger in CD tasks.

Experimental results indicate that SChanger surpasses all benchmark models across multiple datasets, demonstrating notable efficiency, robustness, and scalability. These findings suggest that SChanger has the potential to serve as a benchmark for CD tasks. Future work, from the data perspective, will focus on exploring semisupervised CD, as well as zero-shot and few-shot CD techniques, to further enhance the model's adaptability and performance in scenarios with limited labeled data. From the model perspective, the focus will be on extending the model's capability to handle multitemporal images.

## REFERENCES

- [1] A. Singh, "Review article digital change detection techniques using remotely-sensed data," *Int. J. Remote Sens.*, vol. 10, no. 6, pp. 989–1003, 1989.
- [2] D. Wen et al., "Change detection from very-high-spatial-resolution optical remote sensing images: Methods, applications, and future directions," *IEEE Geosci. Remote Sens. Mag.*, vol. 9, no. 4, pp. 68–101, Dec. 2021.
- [3] Z. Zheng, Y. Zhong, J. Wang, A. Ma, and L. Zhang, "Building damage assessment for rapid disaster response with a deep object-based semantic change detection framework: From natural disasters to man-made disasters," *Remote Sens. Environ.*, vol. 265, 2021, Art. no. 112636.
- [4] Q. Zhu et al., "Land-use/land-cover change detection based on a siamese global learning framework for high spatial resolution remote sensing imagery," *ISPRS J. Photogrammetry Remote Sens.*, vol. 184, pp. 63–78, 2022.
- [5] R. C. Daudt, B. L. Saux, and A. Boulch, "Fully convolutional siamese networks for change detection," in *Proc. IEEE 25th Int. Conf. Image Process.*, 2018, pp. 4063–4067.
- [6] S. Fang, K. Li, and Z. Li, "Changer: Feature interaction is what you need for change detection," *IEEE Trans. Geosci. Remote Sens.*, vol. 61, 2023, Art. no. 5610111.
- [7] S. Zhao, X. Zhang, P. Xiao, and G. He, "Exchanging dual-encoder-decoder: A new strategy for change detection with semantic guidance and spatial localization," *IEEE Trans. Geosci. Remote Sens.*, vol. 61, 2023, Art. no. 4508016.
- [8] W. G. C. Bandara and V. M. Patel, "A transformer-based siamese network for change detection," in *Proc. IEEE Int. Geosci. Remote Sens. Symp.*, 2022, pp. 207–210.
- [9] H. Chen, Z. Qi, and Z. Shi, "Remote sensing image change detection with transformers," *IEEE Trans. Geosci. Remote Sens.*, vol. 60, 2022, Art. no. 5607514.
- [10] S. Zhao, Hao. Chen, X. Zhang, P. Xiao, Lei. Bai, and W. Ouyang, "RS-Mamba for Large Remote Sensing Image Dense Prediction," *IEEE Trans. Geoscie. Remote Sens.*, pp. 1–14, 2024, doi: 10.1109/TGRS.2024.3425540.
- [11] H. Chen and Z. Shi, "A spatial-temporal attention-based method and a new dataset for remote sensing image change detection," *Remote Sens.*, vol. 12, no. 10, 2020, Art. no. 1662.
- [12] M. Lebedev, Y. V. Vizilter, O. Vygolov, V. A. Knyaz, and A. Y. Rubis, "Change detection in remote sensing images using conditional adversarial networks," *Int. Arch. Photogrammetry, Remote Sens. Spatial Inf. Sci.*, vol. 42, pp. 565–571, 2018.

- [13] Y. Long, G.-S. Xia, W. Yang, L. Zhang, and D. Li, "Toward dataset construction for remote sensing image interpretation," in *Proc. IEEE Int. Geosci. Remote Sens. Symp.*, 2021, pp. 1210–1213.
- [14] S. Ji, S. Wei, and M. Lu, "Fully convolutional networks for multisource building extraction from an open aerial and satellite imagery data set," *IEEE Trans. Geosci. Remote Sens.*, vol. 57, no. 1, pp. 574–586, Jan. 2019.
- [15] E. Maggiori, Y. Tarabalka, G. Charpiat, and P. Alliez, "Can semantic labeling methods generalize to any city? The Inria aerial image labeling benchmark," in *Proc. IEEE Int. Geosci. Remote Sens. Symp.*, 2017, pp. 3226–3229.
- [16] O. Russakovsky et al., "ImageNet large scale visual recognition challenge," *Int. J. Comput. Vis.*, vol. 115, pp. 211–252, 2015.
- [17] T.-Y. Lin et al., "Microsoft coco: Common objects in context," in *Proc. 13th Eur. Conf. Comput. Vis.*, Zurich, Switzerland, Sep. 2014, pp. 740–755.
- [18] Y. Xing, J. Jiang, J. Xiang, E. Yan, Y. Song, and D. Mo, "LightCDNet: Lightweight change detection network based on VHR images," *IEEE Geosci. Remote Sens. Lett.*, vol. 20, 2023, Art. no. 2504105.
- [19] C. Zhang et al., "A deeply supervised image fusion network for change detection in high resolution bi-temporal remote sensing images," *ISPRS J. Photogrammetry Remote Sens.*, vol. 166, pp. 183–200, 2020.
- [20] S. J. Pan and Q. Yang, "A survey on transfer learning," *IEEE Trans. Knowl. Data Eng.*, vol. 22, no. 10, pp. 1345–1359, Oct. 2010.
- [21] D. Wang, J. Zhang, B. Du, G.-S. Xia, and D. Tao, "An empirical study of remote sensing pretraining," *IEEE Trans. Geosci. Remote Sens.*, vol. 61, 2023, Art. no. 5608020.
- [22] K. He, X. Zhang, S. Ren, and J. Sun, "Deep residual learning for image recognition," in *Proc. IEEE Conf. Comput. Vis. Pattern Recognit.*, 2016, pp. 770–778.
- [23] Z. Liu et al., "Swin transformer: Hierarchical vision transformer using shifted windows," in *Proc. IEEE/CVF Int. Conf. Comput. Vis.*, 2021, pp. 10012–10022.
- [24] F. Bastani, P. Wolters, R. Gupta, J. Ferdinando, and A. Kembhavi, "SatlasPretrain: A large-scale dataset for remote sensing image understanding," in *Proc. IEEE/CVF Int. Conf. Comput. Vis.*, 2023, pp. 16772–16782.
- [25] D. Wang et al., "MTP: Advancing remote sensing foundation model via multi-task pretraining," *IEEE J. Sel. Topics Appl. Earth Observ. Remote Sens.*, vol. 17, pp. 11632–11654, 2024.
- [26] Y. Cong et al., "SatMAE: Pre-training transformers for temporal and multi-spectral satellite imagery," in *Proc. Int. Conf. Adv. Neural Inf. Process. Syst.*, 2022, vol. 35, pp. 197–211.
- [27] Z. Zheng, A. Ma, L. Zhang, and Y. Zhong, "Change is everywhere: Single-temporal supervised object change detection in remote sensing imagery," in *Proc. IEEE/CVF Int. Conf. Comput. Vis.*, 2021, pp. 15193–15202.
- [28] Z. Zheng, S. Ermon, D. Kim, L. Zhang, and Y. Zhong, "Changen2: Multi-Temporal Remote Sensing Generative Change Foundation Model," *IEEE Trans. Pattern Anal. Mach. Intell.*, vol. 47, no. 2, pp. 725–741, doi: [10.1109/TPAMI.2024.3475824](https://doi.org/10.1109/TPAMI.2024.3475824).
- [29] Y.-X. Wang, D. Ramanan, and M. Hebert, "Growing a brain: Fine-tuning by increasing model capacity," in *Proc. IEEE Conf. Comput. Vis. Pattern Recognit.*, 2017, pp. 2471–2480.
- [30] S.-A. Rebuffi, H. Bilen, and A. Vedaldi, "Learning multiple visual domains with residual adapters," in *Proc. Int. Conf. Adv. Neural Inf. Process. Syst.*, 2017, vol. 30, pp. 506–516.
- [31] Y.-L. Sung, J. Cho, and M. Bansal, "LST: Ladder side-tuning for parameter and memory efficient transfer learning," in *Proc. Int. Conf. Adv. Neural Inf. Process. Syst.*, 2022, vol. 35, pp. 12991–13005.
- [32] K. Li, X. Cao, and D. Meng, "A new learning paradigm for foundation model-based remote-sensing change detection," *IEEE Trans. Geosci. Remote Sens.*, vol. 62, 2024, Art. no. 5610112.
- [33] Z. Zheng, Y. Zhong, A. Ma, and L. Zhang, "Single-temporal supervised learning for universal remote sensing change detection," *Int. J. Comput. Vis.*, vol. 132, pp. 5582–5602, 2024.
- [34] Q. Wang, S. Liu, J. Chanussot, and X. Li, "Scene classification with recurrent attention of VHR remote sensing images," *IEEE Trans. Geosci. Remote Sens.*, vol. 57, no. 2, pp. 1155–1167, Feb. 2019.
- [35] H. Zhai, H. Zhang, P. Li, and L. Zhang, "Hyperspectral image clustering: Current achievements and future lines," *IEEE Geosci. Remote Sens. Mag.*, vol. 9, no. 4, pp. 35–67, Dec. 2021.
- [36] A. Varghese, J. Gubbi, A. Ramaswamy, and P. Balamuralidhar, "ChangeNet: A deep learning architecture for visual change detection," in *Proc. Eur. Conf. Comput. Vis. Workshops*, 2018, pp. 129–145.
- [37] D. Peng, Y. Zhang, and H. Guan, "End-to-end change detection for high resolution satellite images using improved UNet," *Remote Sens.*, vol. 11, no. 11, 2019, Art. no. 1382.
- [38] Y. Zhang, L. Fu, Y. Li, and Y. Zhang, "HDFNet: Hierarchical dynamic fusion network for change detection in optical aerial images," *Remote Sens.*, vol. 13, no. 8, 2021, Art. no. 1440.
- [39] M. Papadomanolaki, S. Verma, M. Vakalopoulou, S. Gupta, and K. Karantzalos, "Detecting urban changes with recurrent neural networks from multitemporal sentinel-2 data," in *Proc. IEEE Int. Geosci. Remote Sens. Symp.*, 2019, pp. 214–217.
- [40] Z. Zheng, Y. Wan, Y. Zhang, S. Xiang, D. Peng, and B. Zhang, "CLNet: Cross-layer convolutional neural network for change detection in optical remote sensing imagery," *ISPRS J. Photogrammetry Remote Sens.*, vol. 175, pp. 247–267, 2021.
- [41] P. Chen, B. Zhang, D. Hong, Z. Chen, X. Yang, and B. Li, "FC-CDN: Feature constraint network for VHR image change detection," *ISPRS J. Photogrammetry Remote Sens.*, vol. 187, pp. 101–119, 2022.
- [42] A. Dosovitskiy, "An image is worth 16x16 words: Transformers for image recognition at scale," in *Proc. Int. Conf. Learn. Representations*, 2021. [Online]. Available: <https://openreview.net/forum?id=YicbFdNTTy>
- [43] H. Bao, L. Dong, S. Piao, and F. Wei, "BEIT: BERT pre-training of image transformers," in *Proc. Int. Conf. Learn. Representations*, 2022. [Online]. Available: <https://openreview.net/forum?id=p-BhZSz59o4>
- [44] F. Yu and V. Koltun, "Multi-scale context aggregation by dilated convolutions," in *Proc. Int. Conf. Learn. Representations*, 2016.
- [45] M. Zhang, G. Xu, K. Chen, M. Yan, and X. Sun, "Triplet-based semantic relation learning for aerial remote sensing image change detection," *IEEE Geosci. Remote Sens. Lett.*, vol. 16, no. 2, pp. 266–270, Feb. 2019.
- [46] Z. Liu, H. Mao, C.-Y. Wu, C. Feichtenhofer, T. Darrell, and S. Xie, "A convnet for the 2020s," in *Proc. IEEE/CVF Conf. Comput. Vis. Pattern Recognit.*, 2022, pp. 11976–11986.
- [47] X. Ding, X. Zhang, J. Han, and G. Ding, "Scaling up your kernels to 31x31: Revisiting large kernel design in CNNs," in *Proc. IEEE/CVF Conf. Comput. Vis. Pattern Recognit.*, 2022, pp. 11963–11975.
- [48] M.-H. Guo, C.-Z. Lu, Z.-N. Liu, M.-M. Cheng, and S.-M. Hu, "Visual attention network," *Comput. Vis. Media*, vol. 9, no. 4, pp. 733–752, 2023.
- [49] S. Shen, Z. Yao, A. Gholami, M. Mahoney, and K. Keutzer, "PowerNorm: Rethinking batch normalization in transformers," in *Proc. Int. Conf. Mach. Learn.*, 2020, pp. 8741–8751.
- [50] J. L. Ba, J. R. Kiros, and G. E. Hinton, "Layer normalization," 2016, [arXiv:1607.06450](https://arxiv.org/abs/1607.06450).
- [51] M. Sandler, A. Howard, M. Zhu, A. Zhmoginov, and L.-C. Chen, "MobileNetV2: Inverted residuals and linear bottlenecks," in *Proc. IEEE Conf. Comput. Vis. Pattern Recognit.*, 2018, pp. 4510–4520.
- [52] J. Hu, L. Shen, and G. Sun, "Squeeze-and-excitation networks," in *Proc. IEEE Conf. Comput. Vis. Pattern Recognit.*, 2018, pp. 7132–7141.
- [53] G. Huang, Y. Sun, Z. Liu, D. Sedra, and K. Q. Weinberger, "Deep networks with stochastic depth," in *Proc. 14th Eur. Conf. Comput. Vis.*, Amsterdam, The Netherlands, Oct. 2016, pp. 646–661.
- [54] X. Qin, Z. Zhang, C. Huang, M. Dehghan, O. R. Zaiane, and M. Jagersand, "U2-Net: Going deeper with nested U-structure for salient object detection," *Pattern Recognit.*, vol. 106, 2020, Art. no. 107404.
- [55] O. Ronneberger, P. Fischer, and T. Brox, "U-Net: Convolutional networks for biomedical image segmentation," in *Proc. 18th Int. Conf. Med. Image Comput. Comput.-Assist. Interv.*, Munich, Germany, Oct. 2015, pp. 234–241.
- [56] K. He, H. Fan, Y. Wu, S. Xie, and R. Girshick, "Momentum contrast for unsupervised visual representation learning," in *Proc. IEEE/CVF Conf. Comput. Vis. Pattern Recognit.*, 2020, pp. 9729–9738.
- [57] L. Shen et al., "S2Looking: A satellite side-looking dataset for building change detection," *Remote Sens.*, vol. 13, no. 24, 2021, Art. no. 5094.
- [58] Q. Shi, M. Liu, S. Li, X. Liu, F. Wang, and L. Zhang, "A deeply supervised attention metric-based network and an open aerial image dataset for remote sensing change detection," *IEEE Trans. Geosci. Remote Sens.*, vol. 60, 2021, Art. no. 5604816.
- [59] J. Ansel et al., "Pytorch 2: Faster machine learning through dynamic python bytecode transformation and graph compilation," in *Proc. 29th ACM Int. Conf. Archit. Support Program. Lang. Operating Syst.*, 2024, vol. 2, pp. 929–947.
- [60] P. Tillet, H.-T. Kung, and D. Cox, "Triton: An intermediate language and compiler for tiled neural network computations," in *Proc. 3rd ACM SIGPLAN Int. Workshop Mach. Learn. Program. Lang.*, 2019, pp. 10–19.
- [61] I. Loshchilov et al., "Fixing weight decay regularization in Adam," in *Proc. Int. Conf. Learning Representations*, 2019. [Online]. Available: <https://openreview.net/forum?id=Bkg6RiCqY7>

- [62] Y. Liu, C. Pang, Z. Zhan, X. Zhang, and X. Yang, "Building change detection for remote sensing images using a dual-task constrained deep Siamese convolutional network model," *IEEE Geosci. Remote Sens. Lett.*, vol. 18, no. 5, pp. 811–815, May 2021.
- [63] C. Han, C. Wu, H. Guo, M. Hu, and H. Chen, "HANet: A hierarchical attention network for change detection with bitemporal very-high-resolution remote sensing images," *IEEE J. Sel. Topics Appl. Earth Observ. Remote Sens.*, vol. 16, pp. 3867–3878, 2023.
- [64] C. Han, C. Wu, H. Guo, M. Hu, J. Li, and H. Chen, "Change guiding network: Incorporating change prior to guide change detection in remote sensing imagery," *IEEE J. Sel. Topics Appl. Earth Observ. Remote Sens.*, vol. 16, pp. 8395–8407, 2023.
- [65] C. Han, C. Wu, M. Hu, J. Li, and H. Chen, "C2F-SemiCD: A coarse-to-fine semi-supervised change detection method based on consistency regularization in high-resolution remote-sensing images," *IEEE Trans. Geosci. Remote Sens.*, vol. 62, 2024, Art. no. 4702621.
- [66] H. Chen, X. Xu, and F. Pu, "SRC-Net: Bi-temporal spatial relationship concerned network for change detection," *IEEE J. Sel. Topics Appl. Earth Observ. Remote Sens.*, vol. 17, pp. 11339–11351, 2024.
- [67] F. Liu, Y. Liu, J. Liu, X. Tang, and L. Xiao, "Candidate-aware and change-guided learning for remote sensing change detection," *IEEE Trans. Geosci. Remote Sens.*, vol. 62, 2024, Art. no. 5624919.
- [68] H. Zhang, G. Ma, and Y. Zhang, "Intelligent-BCD: A novel knowledge-transfer building change detection framework for high-resolution remote sensing imagery," *IEEE J. Sel. Topics Appl. Earth Observ. Remote Sens.*, vol. 15, pp. 5065–5075, 2022.
- [69] X. Liu et al., "MutSimNet: Mutually reinforcing similarity learning for RS image change detection," *IEEE Trans. Geosci. Remote Sens.*, vol. 62, 2024, Art. no. 4403613.
- [70] Q. Li, R. Zhong, X. Du, and Y. Du, "TransUNetCD: A hybrid transformer network for change detection in optical remote-sensing images," *IEEE Trans. Geosci. Remote Sens.*, vol. 60, 2022, Art. no. 5622519.
- [71] W. Luo, Y. Li, R. Urtasun, and R. Zemel, "Understanding the effective receptive field in deep convolutional neural networks," in *Proc. Int. Conf. Adv. Neural Inf. Process. Syst.*, 2016, vol. 29, pp. 4905–4913.
- [72] R. R. Selvaraju, M. Cogswell, A. Das, R. Vedantam, D. Parikh, and D. Batra, "Grad-CAM: Visual explanations from deep networks via gradient-based localization," in *Proc. IEEE Int. Conf. Comput. Vis.*, 2017, pp. 618–626.
- [73] M. Luo, S. Ji, and S. Wei, "A diverse large-scale building dataset and a novel plug-and-play domain generalization method for building extraction," *IEEE J. Sel. Topics Appl. Earth Observ. Remote Sens.*, vol. 16, pp. 4122–4138, 2023.
- [74] V. Mnih, "Machine learning for aerial image labeling," Ph.D. dissertation, Graduate Dep. Comput. Sci., Univ. of Toronto, Toronto, ON, Canada, 2013.
- [75] Z. Wang, Z. Dai, B. Póczos, and J. Carbonell, "Characterizing and avoiding negative transfer," in *Proc. IEEE/CVF Conf. Comput. Vis. Pattern Recognit.*, 2019, pp. 11293–11302.



**Ziyu Zhou** (Student Member, IEEE) is currently working toward the B.S. degree in surveying and mapping engineering with the School of Earth Sciences and Engineering, Hohai University, Nanjing, China.

His research interests include deep learning in remote sensing, change detection, and generative models.



**Keyan Hu** received the B.S. degree in surveying and mapping engineering from the School of Earth Sciences and Engineering, Hohai University, Nanjing, China, in 2024. He is currently working toward the M.S. degree in photogrammetry and remote sensing with the School of Geosciences and Info-Physics, Central South University, Changsha, China.

His research interests include deep learning applications in remote sensing image semantic segmentation, multimodal learning, and generative models.



**Yutian Fang** is currently working toward the B.S. degree in surveying and mapping engineering with the School of Earth Sciences and Engineering, Hohai University, Nanjing, China.

Her research interests include deep learning applications in remote sensing image semantic segmentation, multimodal learning, and generative models.



**Xiaoping Rui** received the Ph.D. degree in cartography and geographic information system from the Graduate University of Chinese Academy of Sciences, Beijing, China, in 2004.

He is currently a Full Professor with the School of Earth Sciences and Engineering, Hohai University, Nanjing, China. His research interests include geographical Big Data mining, 3-D visualization of spatial data, and remote sensing image understanding.